



# Curved Wide Plate Test Results and Transferability of Test Specimens

## Topical Report 277-T-11

For Project

# Weld Design, Testing, and Assessment Procedures for High Strength Pipelines

### Prepared for the

Design, Materials, and Construction Technical Committee of  
Pipeline Research Council International, Inc.  
Project MATH-1 Catalog No. L5XXXX

and

U.S. Department of Transportation  
Pipeline and Hazardous Materials Safety Administration  
Office of Pipeline Safety  
Agreement Number DTPH56-07-T-000005

### Prepared by

Center for Reliable Energy Systems  
Yong-Yi Wang and Honggang (Michael) Zhou

### Assisted by

Bill Tyson Jim Gianetto—CANMET Materials Technology Laboratory,  
Marie Quintana—Lincoln Electric Company,  
Timothy Weeks—National Institute of Standards and Technology

January 21, 2012

This research was funded in part under the Department of Transportation, Pipeline and Hazardous Materials Safety Administration's Pipeline Safety Research and Development Program. The views and conclusions contained in this document are those of the authors and should not be interpreted as representing the official policies, either expressed or implied, of the Pipeline and Hazardous Materials Safety Administration, or the U.S. Government.

Contribution of an agency of the U.S. government, not subject to copyright



Catalog No. L5XXXX

# **Curved Wide Plate Test Results and Transferability of Test Specimens**

## **Topical Report 277-T-07**

For Project

# **Weld Design, Testing, and Assessment Procedures for High Strength Pipelines**

### **Prepared for the**

Design, Materials, and Construction Technical Committee of  
Pipeline Research Council International, Inc.  
Project MATH-1 Catalog No. L5XXXX

and

U.S. Department of Transportation  
Pipeline and Hazardous Materials Safety Administration  
Office of Pipeline Safety  
Agreement Number DTPH56-07-T-000005

### **Prepared by**

Center for Reliable Energy Systems  
Yong-Yi Wang and Honggang (Michael) Zhou

### **Assisted by**

Bill Tyson Jim Gianetto/CANMET,  
Marie Quintana/Lincoln,  
Timothy Weeks/NIST

Version	Date of Last Revision	Date of Uploading	Comments
Draft	April 23, 2011	April 23, 2011	
2.0	December 17, 2011		
Final	January 21, 2012		

This report is furnished to Pipeline Research Council International, Inc. (PRCI) under the terms of PRCI contract [277-PR-348-074512] between PRCI and the MATH-1 contractors:

- Electricore (prime contractor),
- Center for Reliable Energy Systems, CANMET, NIST, and The Lincoln Electric Company (sub-contractors).

The contents of this report are published as received from the MATH-1 contractor and subcontractors. The opinions, findings, and conclusions expressed in the report are those of the authors and not necessarily those of PRCI, its member companies, or their representatives. Publication and dissemination of this report by PRCI should not be considered an endorsement by PRCI of the MATH-1 contractor and subcontractors, or the accuracy or validity of any opinions, findings, or conclusions expressed herein.

In publishing this report, PRCI and the MATH-1 contractors make no warranty or representation, expressed or implied, with respect to the accuracy, completeness, usefulness, or fitness for purpose of the information contained herein, or that the use of any information, method, process, or apparatus disclosed in this report may not infringe on privately owned rights. PRCI and the MATH-1 contractors assume no liability with respect to the use of, or for damages resulting from the use of, any information, method, process, or apparatus disclosed in this report. By accepting the report and utilizing it, you agree to waive any and all claims you may have, resulting from your voluntary use of the report, against PRCI and the MATH-1 contractors.

Pipeline Research Council International Catalog No. L5XXXX

PRCI Reports are Published by Technical Toolboxes, Inc.

3801 Kirby Drive, Suite 520  
Houston, Texas 77098  
Tel: 713-630-0505  
Fax: 713-630-0560  
Email: [info@ttoolboxes.com](mailto:info@ttoolboxes.com)

## PROJECT PARTICIPANTS

<b>PROJECT TEAM MEMBER</b>	<b>COMPANY AFFILIATION</b>	<b>PROJECT TEAM MEMBER</b>	<b>COMPANY AFFILIATION</b>
Arti Bhatia	Alliance	Jim Costain	GE
Jennifer Klementis	Alliance	Gilmar Batista	Petrobras
Roger Haycraft	Boardwalk	Marcy Saturno de Menezes	Petrobras
David Horsley	BP	Dave Aguiar	PG&E
Mark Hudson	BP	Ken Lorang	PRCI
Ron Shockley	Chevron	Maslat Al-Waranbi	Saudi Aramco
Sam Mishael	Chevron	Paul Lee	SoCalGas
David Wilson	ConocoPhillips	Alan Lambeth	Spectra
Satish Kulkarni	El Paso	Robert Turner	Stupp
Art Meyer	Enbridge	Gilles Richard	TAMSA
Bill Forbes	Enbridge	Noe Mota Solis	TAMSA
Scott Ironside	Enbridge	Philippe Darcis	TAMSA
Sean Keane	Enbridge	Dave Taylor	TransCanada
Laurie Collins	Evraz	Joe Zhou	TransCanada
David de Miranda	Gassco	Jason Skow	TransGas
Adriaan den Herder	Gasunie	Ernesto Cisneros	Tuberia Laguna
Jeff Stetson	GE	Vivek Kashyap	Welspun
		Chris Brown	Williams

<b>CORE RESEARCH TEAM</b>	
<b>RESEARCHER</b>	<b>COMPANY AFFILIATION</b>
Yaoshan Chen	Center for Reliable Energy Systems
Yong-Yi Wang	Center for Reliable Energy Systems
Ming Liu	Center for Reliable Energy Systems
Dave Fink	Lincoln Electric Company
Marie Quintana	Lincoln Electric Company
Vaidyanath Rajan	Lincoln Electric Company
Joe Daniel	Lincoln Electric Company
Radhika Panday	Lincoln Electric Company
James Gianetto	CANMET Materials Technology Laboratory
John Bowker	CANMET Materials Technology Laboratory
Bill Tyson	CANMET Materials Technology Laboratory
Guowu Shen	CANMET Materials Technology Laboratory
Dong Park	CANMET Materials Technology Laboratory
Timothy Weeks	National Institute of Standards and Technology
Mark Richards	National Institute of Standards and Technology
Dave McColskey	National Institute of Standards and Technology
Enrico Lucon	National Institute of Standards and Technology
John Hammond	Consultant Metallurgist & Welding Engineer

**This Page Intentionally Left Blank**

## FINAL REPORT STRUCTURE

<b>Focus Area 1 - Update of Weld Design, Testing, and Assessment Procedures for High Strength Pipelines</b>		
<b>Report #</b>	<b>Description</b>	<b>Lead Authors</b>
277-T-01	Background of Linepipe Specifications	CRES/CANMET
277-T-02	Background of All-Weld Metal Tensile Test Protocol	CANMET/Lincoln
277-T-03	Development of Procedure for Low-Constraint Toughness Testing Using a Single-Specimen Technique	CANMET/CRES
277-T-04	Summary of Publications: Single-Edge Notched Tension SE(T) Tests	CANMET
277-T-05	Small Scale Tensile, Charpy V-Notch, and Fracture Toughness Tests	CANMET/NIST
277-T-06	Small Scale Low Constraint Fracture Toughness Test Results	CANMET/NIST
277-T-07	Small Scale Low Constraint Fracture Toughness Test Discussion and Analysis	CANMET/NIST
277-T-08	Summary of Mechanical Properties	CANMET
277-T-09	Curved Wide Plate Tests	NIST/CRES
277-T-10	Weld Strength Mismatch Requirements	CRES/CANMET
277-T-11	Curved Wide Plate Test Results and Transferability of Test Specimens	CRES/CANMET
277-S-01	Summary Report 277 Weld Design, Testing, and Assessment Procedures for High Strength Pipelines	CRES

<b>Focus Area 2 - Development of Optimized Welding Solutions for X100 Linepipe Steel</b>		
<b>Report #</b>	<b>Description</b>	<b>Lead Authors</b>
278-T-01	State of The Art Review	Lincoln
278-T-02	Material Selection, Welding and Weld Monitoring	Lincoln/CANMET
278-T-03	Microstructure and Hardness Characterization of Girth Welds	CANMET/Lincoln
278-T-04	Microstructure and Properties of Simulated Weld Metals	CANMET/Lincoln
278-T-05	Microstructure and Properties of Simulated Heat Affected Zones	CANMET/Lincoln
278-T-06	Essential Welding Variables	Lincoln/CANMET
278-T-07	Thermal Model for Welding Simulations	CRES/CANMET
278-T-08	Microstructure Model for Welding Simulations	CRES/CANMET
278-T-09	Application to Other Processes	Lincoln/CANMET
278-S-01	Summary Report 278 Development of Optimized Welding Solutions for X100 Line Pipe Steel	Lincoln

## **EXECUTIVE SUMMARY**

The work described in this report focuses on the development of data processing routines for curved-wide-plate (CWP) tests, the presentation of test results in a consistent and unified format, generation of fracture resistance curves from, and the examination of transferability between CWP and SENT (single-edge-notched tension) test specimens. The results of this work can be used for:

- Drafting and implementing consistent test procedures for CWP tests,
- Formulating test data for consistent presentation and comparison,
- Understanding the differences and limitations of test specimens of different scales,
- Making the best selection of test specimens for a given set of objectives, and
- Making correct interpretation of test data and their relevance to girth weld performance.

A variety of mechanical property tests are performed in the design, construction and maintenance phase of a pipeline. Most of the tests are done using small-scale specimens with the size typically in the range of a few inches to tens of inches. There is a wide selection of test labs for most small-scale tests. These tests can be done effectively under a variety of conditions, e.g., test temperature, strain rate, and loading configuration. More importantly, most routine small-scale tests are done in accordance with national and international standards so the consistency of testing procedure is usually very good.

To confirm pipeline designs and validate material performance, it's desirable sometimes to test girth welds under realistic service conditions in full scale. Full-scale tests can incorporate certain realistic features that the small-scale specimens cannot. However, these tests can be time-consuming and expensive to conduct. Very few labs can do the tests, even with months of start-up and preparation time. There are no generally accepted consistent test procedures among different test labs. The data acquisition and post-processing may differ from lab to lab, creating difficulties in data comparison. Full-scale tests can only be done under selected conditions as a supplemental tool to the small-scale tests. The amount of resources and time required to conduct such tests prevent them becoming routine tests.

The medium-scale tests, represented by curved-wide-plate (CWP) tests, offer certain advantages associated with full-scale tests at a fraction of the cost of full-scale tests. A large number of CWP tests were conducted within this project. Procedures developed in this project enable the generation of resistance curves from CWP specimens. Another major outcome of this work is the implementation of a uniform presentation format for all CWP test data.

A few major observations are

- 1) It is possible to obtain highly consistent data representing the deformation of CWP specimens.
- 2) Based on the compliance and flaw growth history data, most of the flaw growth occurs near the final failure strain. The amount of flaw growth at a strain level up to 90% of the final failure strain is a small fraction of the total flaw growth at failure.
- 3) From a practical viewpoint of tensile strain design, it is advisable to use flaw growth initiation as a failure criterion. The benefits of a small increase in strain capacity do not justify the risk associated with allowing a large amount of flaw growth.
- 4) Despite a highly diligent and meticulous effort of post-test data processing, the scatter of the experimentally measured compliance of CWP specimens makes it difficult to construct “clean” resistance curves in some cases. This difficulty is particularly pronounced in the initial part of the resistance curves.
- 5) For cases when “clean” resistance curves can be established, the resistance curves from CWP tests are generally higher than those from SENT tests. The difference is more pronounced after a flaw growth of approximately 1.0 mm. Due to the noise associated with the initial flaw growth, comparison of resistance curves at smaller amount of flaw growth is difficult.
- 6) Post-test data processing to generate resistance curves can be a difficult task. The process can be subject to judgment calls of the individuals who process the data. The use of resistance curve data should be preceded with clearly defined procedures for data processing. The robustness of the raw data prior to data processing should be examined and verified. A significant issue in developing a consistent understanding of the transferability of resistance curves from data in the open literature is the lack of detailed and specific information about the method and procedures used in the acquisition of the raw data and in the post-test data processing of the raw data. Without the necessary and specific information on the procedures leading to the presentation of the final data, such as resistance curves, it is nearly impossible to determine if comparisons and conclusions are drawn on a consistent basis. It is in the interest of all stakeholders that detailed and specific test procedures and data processing routines are provided so the material behavior can be understood.

The work presented here provides means to generate resistance curves from CWP tests. An equally important point is that such an endeavor is not easy. To fully understand the material behavior, it is critical that the test data be presented along with detailed procedures by which the data are derived.

## TABLE OF CONTENTS

EXECUTIVE SUMMARY .....	vii
TABLE OF CONTENTS.....	ix
LIST OF FIGURES .....	x
LIST OF TABLES.....	xi
1 INTRODUCTION AND BACKGROUND .....	1
1.1 BACKGROUND .....	1
1.2 INCENTIVE .....	2
1.3 OBJECTIVE OF THIS WORK.....	3
1.4 SCOPE OF THE REPORT.....	3
2 REVIEW OF PRIOR WORK ON TRANSFERABILITY.....	3
3 CURVED-WIDE-PLATE TEST .....	7
3.1 OVERVIEW .....	7
3.2 TEST SETUP.....	8
3.3 TEST MATRIX.....	12
4 DEVELOPMENT OF COMPLIANCE FUNCTION.....	14
4.1 INTRODUCTION .....	14
4.2 FINITE ELEMENT MODELS.....	14
4.3 RESULTS .....	16
4.4 DISCUSSION.....	18
5 DEVELOPMENT OF <i>J</i> -CORRELATION EQUATIONS.....	18
5.1 INTRODUCTION .....	18
5.2 FINITE ELEMENT MODELS.....	18
5.3 RESULTS .....	22
5.4 DISCUSSION.....	23
6 EXAMINATION OF TEST RESULTS .....	23
6.1 INTRODUCTION .....	23
6.2 SAMPLE TEST DATA.....	24
6.3 SUMMARY OF TEST DATA .....	39
7 COMPARISON OF RESISTANCE CURVES .....	40
7.1 OVERALL ORGANIZATION OF THE DATA .....	40
7.2 SAMPLE RESISTANCE CURVE COMPARISON.....	40
8 CONCLUDING REMARKS.....	46
9 REFERENCES .....	48

## LIST OF FIGURES

Figure 1:	CTOD resistance curves of three types of specimens .....	4
Figure 2:	Dependence of J resistance curves on specimen type and side groove of X100 base pipe [9]. PS: plane-sided (non-side-grooved). SG: side-grooved.....	4
Figure 3:	Measured CTOD R-curves of X65 welds [7].....	5
Figure 4:	Measured CTOD R-curves of X70 base pipe from full-scale (FS), CWP, and SENT specimens [7].....	5
Figure 5:	Comparison of resistance curves between full-scale pipes and SENT specimens.....	7
Figure 6:	A CWP specimen in the test frame of NIST Boulder.....	9
Figure 7:	Dimensions of the CWP specimens.....	10
Figure 8:	Instrumentation plan of the CWP specimens.....	11
Figure 9:	Clip gage arrangement for CMOD measurement.....	12
Figure 10:	A sample finite element model with relevant dimension designation.....	15
Figure 11:	Finite element model in the vicinity of the surface-breaking flaw. The weld metal is shown in red, and the pipe base metal is shown in green .....	15
Figure 12:	Relation between flaw depth and compliance .....	17
Figure 13:	Interpolation coefficients as a function of flaw length (2c).....	17
Figure 14:	Definition of the plastic component of the area under the load versus CMOD curve .....	20
Figure 15:	Schematic description of $\eta$ factor evaluation.....	21
Figure 16:	Load-displacement and CMOD-displacement relation of CWP-11 .....	25
Figure 17:	Description of the cross section area calculation.....	26
Figure 18:	Stress and displacement relation of CWP-11 .....	26
Figure 19:	Remote strain versus displacement above the weld of CWP-11 .....	28
Figure 20:	Remote strain versus displacement below the weld of CWP-11 .....	29
Figure 21:	Strain across the weld versus displacement of CWP-11 .....	29
Figure 22:	Average strain above the weld versus average strain below the weld of CWP-11 .....	30
Figure 23:	Average strain above and below the weld of CWP-11 versus CMOD.....	30
Figure 24:	Average strain across the weld versus CMOD of CWP-11.....	31
Figure 25:	Load-CMOD plot for specimen CWP-11 .....	31
Figure 26:	Compliance versus CMOD of CWP-11 .....	33
Figure 27:	Compliance versus average strain above the weld of CWP-11 .....	33
Figure 28:	Compliance versus average strain below weld of CWP-11.....	34
Figure 29:	CMOD and flaw depth relation of CWP-11 .....	35
Figure 30:	Flaw depth versus strains.....	35
Figure 31:	Stress versus average strain below the weld of CWP-11 .....	36
Figure 32:	Stress versus average strain above the weld of CWP-11.....	36
Figure 33:	CMOD versus average strain below the weld of CWP-11 .....	37
Figure 34:	CMOD versus average strain above the weld of CWP-11 .....	37

Figure 35: Fracture resistance curve of CWP-11 .....	38
Figure 36: CMOD versus applied nominal stress of CWP-11 .....	39
Figure 37: SENT resistance curves of the first round of welds, notch located in the weld metal, a=6 mm and T=-20 °C .....	42
Figure 38: CWP resistance curves of the first round of weld, notch located in the weld metal, a=6 mm and T=-20 °C .....	42
Figure 39: CWP resistance curves versus SENT resistance curves of the first round of weld, weld notch, a=6 mm and T=-20 °C .....	43
Figure 40: SENT resistance curves of the second round of weld, HAZ notch, a=3 mm and T=RT .....	43
Figure 41: CWP resistance curves of the second round of weld, HAZ notch, a=3 mm and T=RT .....	44
Figure 42: CWP resistance curves versus SENT resistance curves of the second round of weld, HAZ notch, a=3 mm and T=RT .....	44
Figure 43: After-test weld cross section macro of CWP-21 of the second round of weld, HAZ notch, a=3 mm and T=RT .....	45
Figure 44: After-test weld cross section macro of CWP-27 of the second round of weld, HAZ notch, a=6 mm and T=-20 °C .....	45
Figure 45: CWP resistance curves versus SENT resistance curves of the second round of weld, HAZ notch, a=6 mm and T=-20 °C .....	46

## LIST OF TABLES

Table 1: CWP test matrix .....	13
Table 2: Analysis matrix for compliance function .....	14
Table 3: Coefficients of the parabolic functions. A1: coefficient of the 2nd order term, A2: coefficient of the 1st order term .....	18
Table 4: Analysis geometry matrix for J-correlation equations .....	19
Table 5: Material property matrix for development of J-correlation equations .....	19
Table 6: Description of the data graphs .....	24
Table 7: CWP-11 response as measured by various parameters as a function of the unloading sequence .....	32
Table 8: Summary of SENT resistance curve versus CWP resistance curve .....	41

# 1 INTRODUCTION AND BACKGROUND

## 1.1 BACKGROUND

A variety of mechanical property tests are performed in the design, construction and maintenance phase of a pipeline. The linepipes are often qualified by tensile, Charpy impact, and DWTT tests, among other tests. Girth welding procedure qualification requires at least cross-weld tensile, side-bend and/or root bend, and/or nick-break tests. For welding procedures qualified for alternative flaw acceptance criteria (alternatively termed ECA, or Engineering Critical Assessment), fracture toughness tests and/or Charpy impact tests are required. These tests are generally referred to as small-scale tests. The size of specimens is typically in the range of a few inches to tens of inches. The specimens are usually small enough to be handled manually without the assistance of any lifting equipment. There is a wide selection of test labs for most small-scale tests. These tests can be done effectively under a variety of conditions, e.g., test temperature, strain rate, and loading configuration. More importantly, most routine small-scale tests are done in accordance with national and international standards so the consistency of testing procedure is usually very good. Having consistent, transparent, and robust test standards ensures that the differences in the test data are attributable to material behavior, not testing procedures themselves.

To confirm pipeline designs and validate material performance, it's desirable sometimes to test girth welds under realistic service conditions in full scale. Full-scale tests can incorporate certain realistic features that the small-scale specimens cannot. These features include, but are not limited to, finite-length surface-breaking flaws, weld high-low misalignment, and internal pressure. Full-scale tests may be necessary to qualify the impact of such features. However, these tests present their own challenges and pitfalls.

- 1) The tests can take months to prepare.
- 2) The tests are very expensive to conduct.
- 3) There is a limited number of test frames capable of handling large-diameter pipes. Sometimes test frames have to be purposely built. These frames may have to be decommissioned when the tests are completed as they take up too much space.
- 4) Certain test conditions, such as low temperature tests, are difficult to achieve uniformly for very large specimens.
- 5) There are no generally accepted consistent test procedures among different test labs. The data acquisition and post-processing may differ from lab to lab, creating difficulties in data comparison.

In summary, full-scale tests can only be done under selected conditions as a supplemental tool to the small-scale tests. The amount of resources and time required to conduct such tests prevent them from becoming routine tests.

Situated in the middle of the specimen size scale is the medium-scale test, such as curved- wide-plate (CWP) test. The CWP specimen is a curved piece of pipe with a nominal gauge width of 200 to 450 mm (8 to 18 inches) and the length in the range of approximately 1.5-6.0 times the gauge width. A girth weld is located in the mid-length of the specimen. In most cases, an artificial machined notch or fatigue sharpened flaw is introduced in the weld centerline or heat-

affected zone (HAZ). The deformation and load are monitored during the tests while the specimen is pulled longitudinally until failure or reaching certain pre-set conditions, such as passing the maximum load.

CWP tests have been used for the characterization of girth weld performance for many years [1,2]. More recently, wide plate tests have become one of the most recognized tools for the determination of girth weld tensile strain capacity. Many organizations now have CWP testing capabilities, for example the University of Gent, C-FER, Stress Engineering Services, National Institute of Standards and Technology (NIST), Evraz, JFE, Nippon Steel Corporation, and POSCO.

In order to use the test specimens of various scales effectively, one has to understand their useful features and limits. One of the critical questions is the transferability of test results, i.e., how the test results from one scale of test specimen can be correlated to the results of another scale of test specimen. This question is not as easy to answer as it seems.

- Ideally tests of different scales can be done to evaluate the transferability. The reality is significantly more challenging. Material properties often have local variations, particularly in welds and HAZ. The test results from nominally the same material and the same test conditions can differ due to those local variations. It is well documented from large-scale tests that flaws under “nominally identical conditions” can behave quite differently [3]. These so-called “identical conditions” refer to the application of well planned and executed procedures to ensure identical conditions with tools that are reasonably controlled. For instance, HAZ flaws can be put in the same target location. However the local micro-scale features can be different from one flaw location to another.
- There are no test standards for medium- and large-scale test specimens. Differences in test results may reflect differences in both material behavior and test procedures.

In summary, the determination of transferability from tests alone can be difficult without conducting a large number of tests, including large-scale tests. Given the time and cost associated with large-scale tests, this line of investigation is seldom pursued. Numerical analysis, in which various parameters can be varied systematically, is a valuable tool to determine the specimen transferability. Such analysis, complemented by selected experimental tests of different scales, is the most effective and practical approach to examine transferability.

## **1.2 INCENTIVE**

Small-scale, CWP, and full-scale tests have been used for many years in the pipeline industry. These tests are being increasingly used in recent years for strain-based design of pipelines, especially for the determination of girth weld behavior under large longitudinal tensile strain. The transferability of these test forms has not been thoroughly investigated. The lack of generally accepted test procedures for the medium- and large-scale specimens further complicated the understanding and comparison of test data.

It is therefore essential to address two interrelated and critical issues: (1) consistent test procedures for the medium- and large-scale specimens and (2) understanding of the transferability of test specimens of different scales.

### **1.3 OBJECTIVE OF THIS WORK**

The overall objectives of this work are as follows:

- 1) Develop critically missing elements for post-test data processing of CWP tests,
- 2) Process and organize CWP test data in a unified and consistent format, and
- 3) Evaluate the transferability of various tests. Since full-scale testing is not conducted within this project, the focus is on the transferability of small-scale test data to prediction of CWP performance.

### **1.4 SCOPE OF THE REPORT**

One of the primary goals of this work is the organization and presentation of CWP test results. One of the key elements of the test results is the fracture resistance curves. To derive the resistance curves from test data, two essential elements have to be established: (1) determination of flaw size from unloading compliance and (2) converting load vs. CMOD trace into fracture mechanics parameters. The transferability in the form of resistance curves can be assessed with the CWP resistance curves.

In Section 2, the transferability of different test specimens, mostly in the form of resistance curves, is reviewed. The CWP test procedures employed in this project are introduced in Section 3. The development of compliance function for the determination of flaw size is covered in Section 4. The development of  $J$  correlation equations is described in Section 5. Sample CWP test data in a uniform format are presented in Section 6. The comparison of resistance curves is made in Section 7. The important findings and concluding remarks are given in Section 8. Due to the large size of data files of the CWP test data, most of the CWP test results will be made available in electronic format.

## **2 REVIEW OF PRIOR WORK ON TRANSFERABILITY**

Material resistance to flaw growth is one of the key input parameters for the tensile strain design of pipeline girth welds. It is useful to evaluate the similitude of resistance curves among specimens of different types. The types of specimens being evaluated are CWP, standard three-point bend CTOD, and low-constraint SENT specimens. CWP has been used as a quasi-structural specimen to evaluate the tensile strain capacity of pipeline girth welds [4,5]. The standard three-point bend CTOD specimen is perhaps the most recognized fracture toughness specimen for girth weld qualification. In recent years the low-constraint SENT specimen is increasingly being used because it is viewed as a more appropriate measure of girth weld loading condition than the SENB specimen [6,7].

The resistance curves from different types of specimen are compared here. In the early tests by SINTEF, the resistance curve of the “Sector” specimen is shown to be the highest, followed by SENT, and then SENB, as shown in Figure 1 [8]. Tests conducted at CANMET show that the resistance curves from SENT are generally higher than those from SENB, as shown in Figure 2 [9]. Cheng et al. showed that the resistance curves of SENT specimens are markedly higher than those of SENB specimens, as shown in Figure 3 [7]. Cheng et al. also showed that there is a

good similitude of resistance curves between the full-scale and SENT specimens, as shown in Figure 4 [7]. The resistance curves of the CWP specimens are somewhat lower than both the SENT and full-scale specimens.

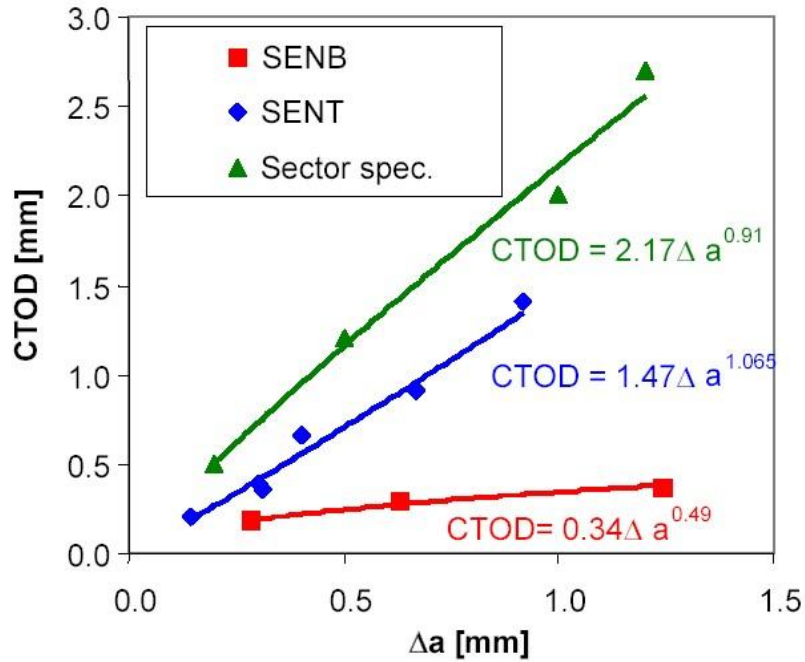


Figure 1: CTOD resistance curves of three types of specimens

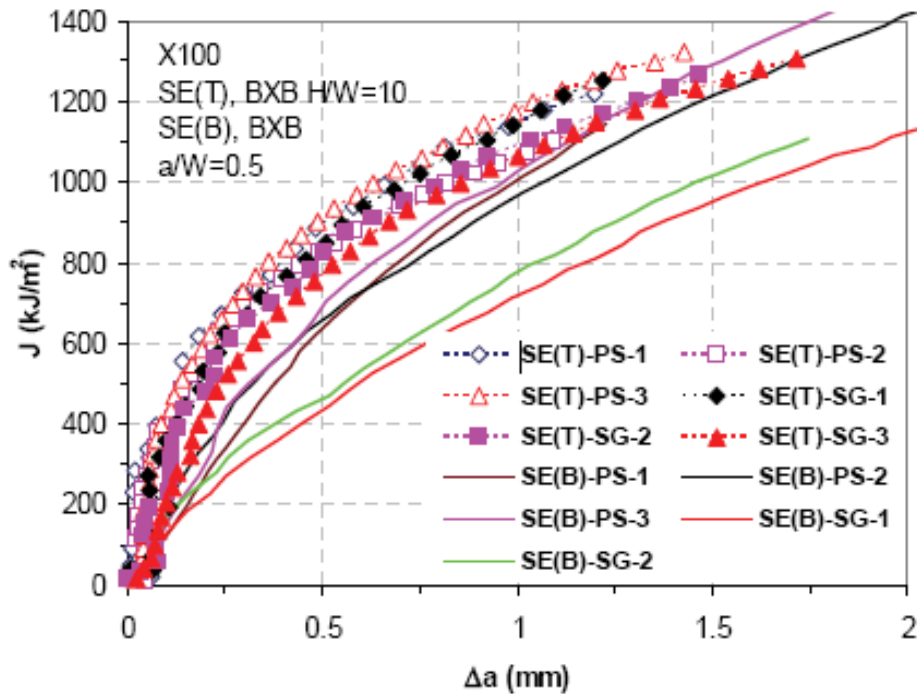


Figure 2: Dependence of J resistance curves on specimen type and side groove of X100 base pipe [9]. PS: plane-sided (non-side-grooved). SG: side-grooved.

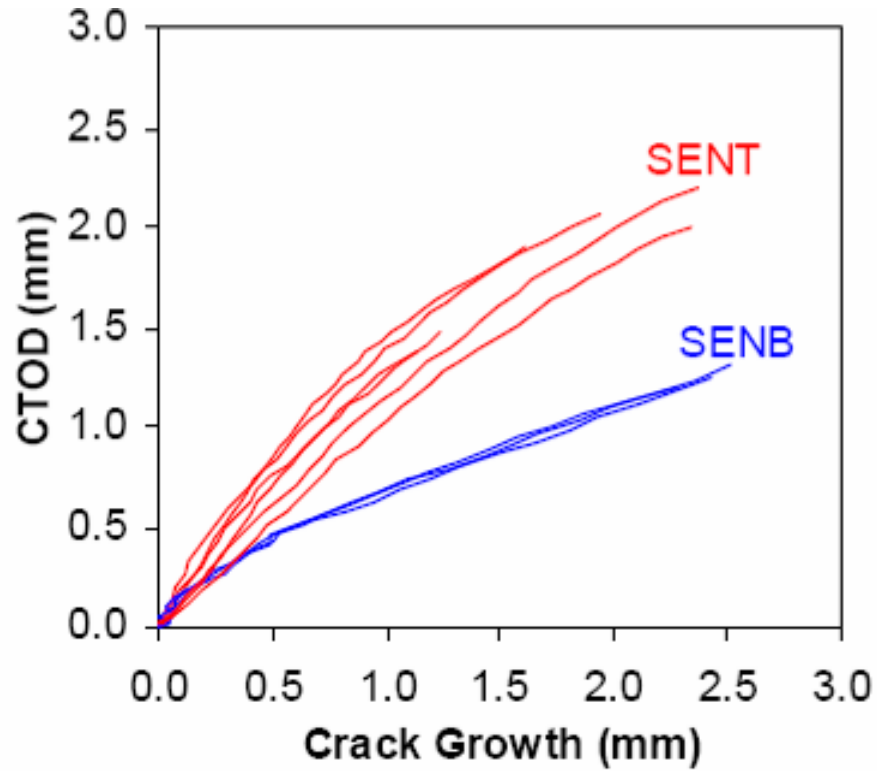


Figure 3: Measured CTOD R-curves of X65 welds [7]

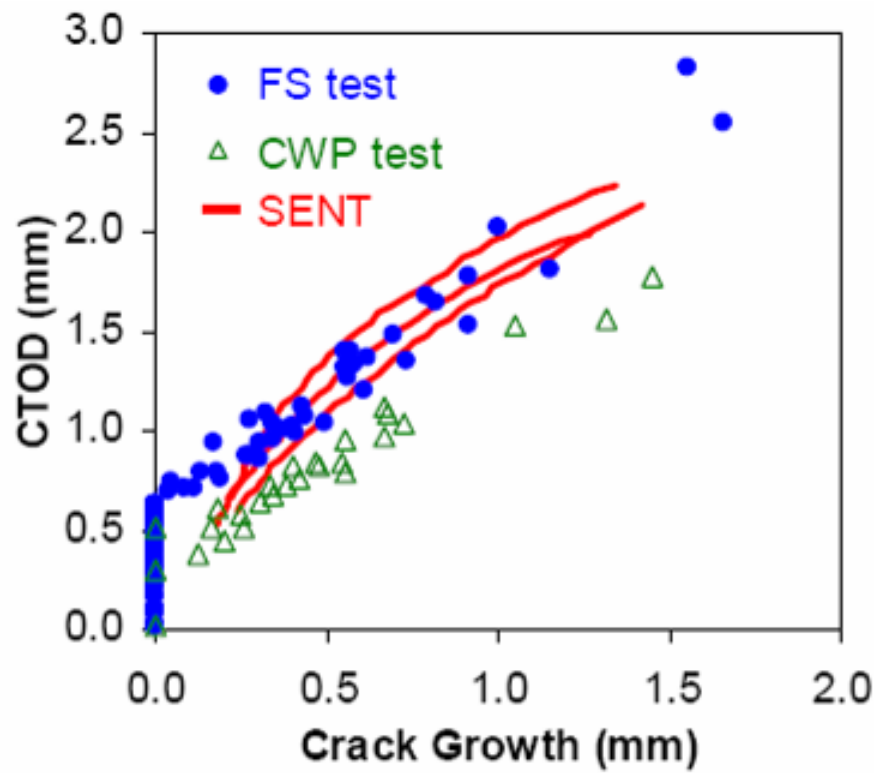


Figure 4: Measured CTOD R-curves of X70 base pipe from full-scale (FS), CWP, and SENT specimens [7]

The transferability of resistance curves between full-scale pipes and SENT specimens was examined in great detail in another DOT/PRCI funded project [10]. Figure 5 shows the comparison of resistance curves between the full-scale pipes and the corresponding SENT tests for six groups of material and flaw locations. The resistance curves of the full-scale pipes are slightly higher than those of SENT specimens in some cases, but significantly higher in other cases. This comparison demonstrates that the transferability of resistance curves between the full-scale pipes and SENT cannot be assured in all cases. This observation is consistent with the philosophy of DNV-RP-F108 and different from the results presented by Cheng et al [7]. The transferability of resistance curves between full-scale pipes and SENT specimens should not be automatically assumed in all cases. More in-depth analysis of past and future data is necessary to establish the transferability.

A significant issue in developing a consistent understanding of the transferability of resistance curves is the lack of detailed and specific information about the methods and procedures used in the acquisition of the raw data and in the post-test processing of the raw data. Without the necessary and specific information on the procedures leading to the presentation of the final data, such as resistance curves, it is nearly impossible to determine if comparisons and conclusions are drawn on a consistent basis. It is in the interest of all stakeholders that detailed and specific tests procedures and data processing routines are provided so the material behavior can be understood.

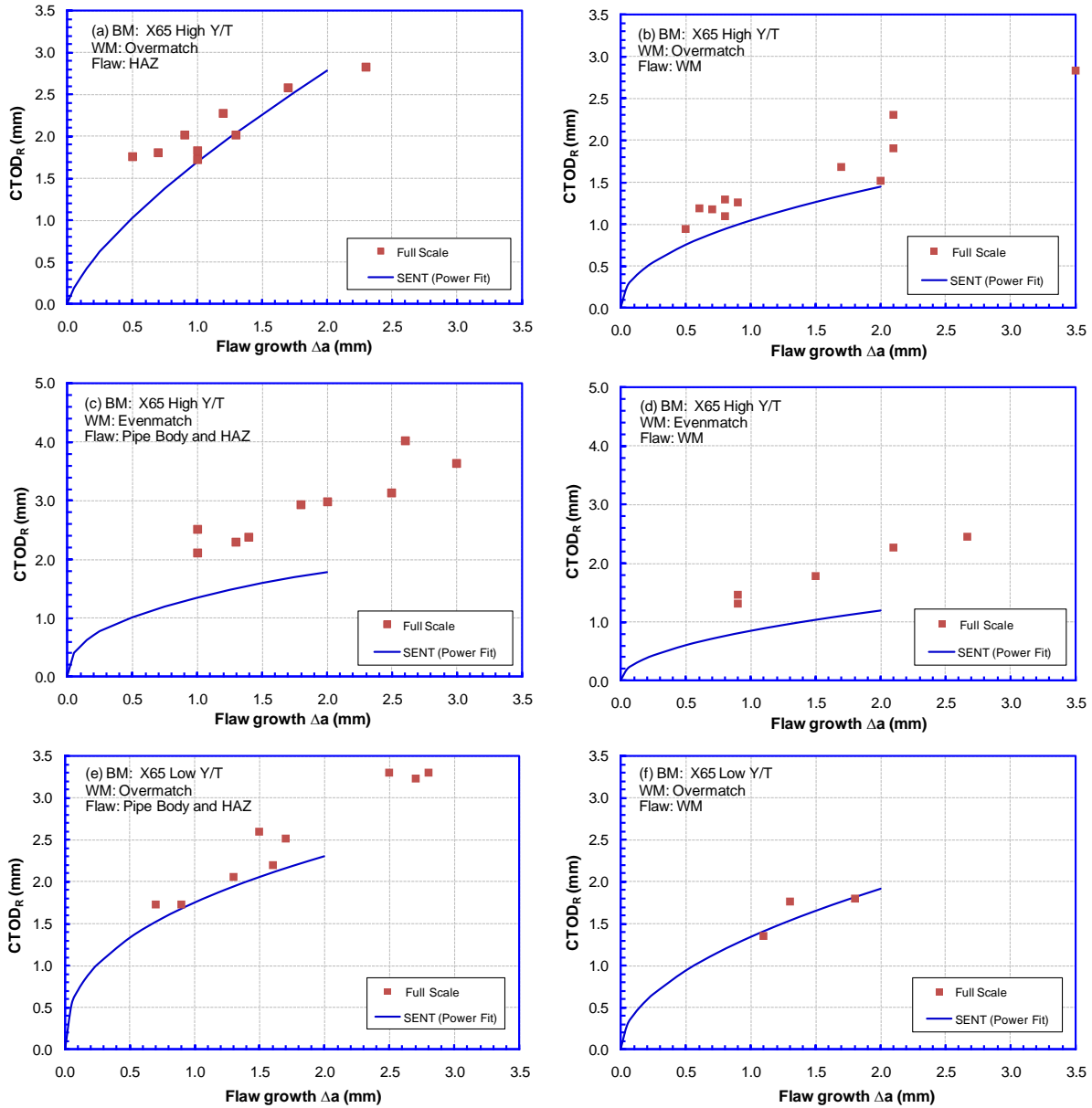


Figure 5: Comparison of resistance curves between full-scale pipes and SENT specimens

### 3 CURVED-WIDE-PLATE TEST

#### 3.1 OVERVIEW

Wide-plate testing has been used as a tool for material and weld procedure qualifications [11]. It has also been used for project-specific design validation. A large database of the failure strains of girth welded pipes has been established from wide-plate tests [12]. There are no generally accepted test standards governing the specimen dimensions, instrumentation, data acquisition and post-test processing. A study has shown that the specimen width, weld strength mismatch, and specimen length have strong impacts on the reported failure strains when the failure strains are measured in the most commonly used form [5]. Significant progress has been made in

recognizing the importance of having consistent test procedures [5]. Denys et al. have published a recommended testing procedure of CWP specimens [13].

A large number of curved-wide-plate tests have been conducted within this project. This report summarizes the preliminary results of the post-test data analysis. A brief introduction of the test setup and instrumentation plan is given here so the processed data can be interpreted in the context of actual measurements taken.

### **3.2 TEST SETUP**

A picture showing a test specimen in the test frame at the NIST Boulder test lab is given in Figure 6. The test machine is of vertical type, capable of a maximum load capacity of 1,000,000 lbf. The overall dimensions of the specimens are given in Figure 7. The gage width of 10 inches was selected to ensure that the maximum load capacity of the specimen can be reached near the maximum load capacity of the test machine.

The overall instrumentation plan is shown in Figure 8. Three high-precision clip gages were installed on the ID side to measure the crack mouth opening displacement (CMOD) as shown in Figure 9. The clip gages are kept in place by the leaf springs pressing the gages against the specimen. More information on the test setup can be found in a companion report [14].



**Figure 6: A CWP specimen in the test frame of NIST Boulder**

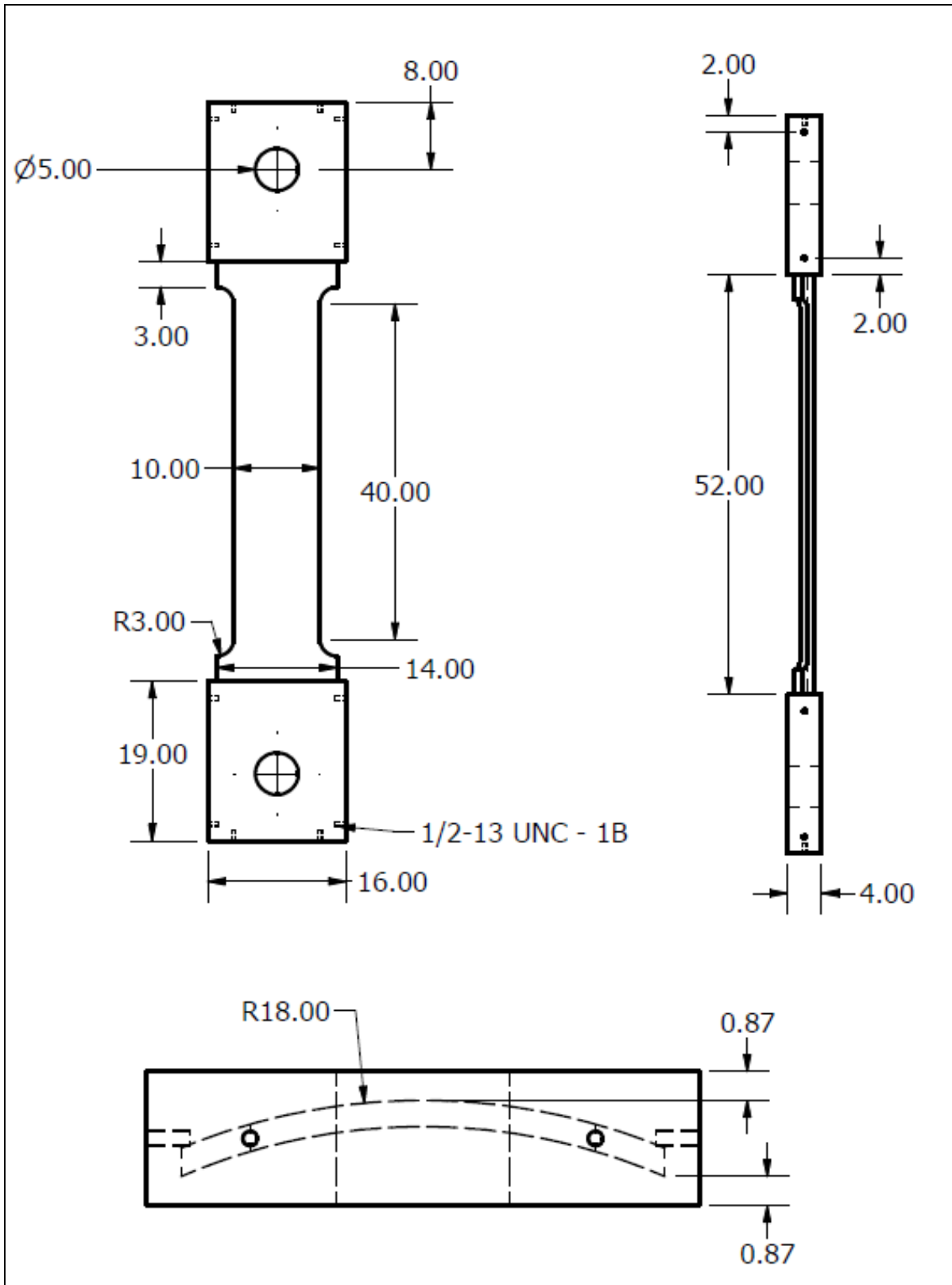


Figure 7: Dimensions of the CWP specimens

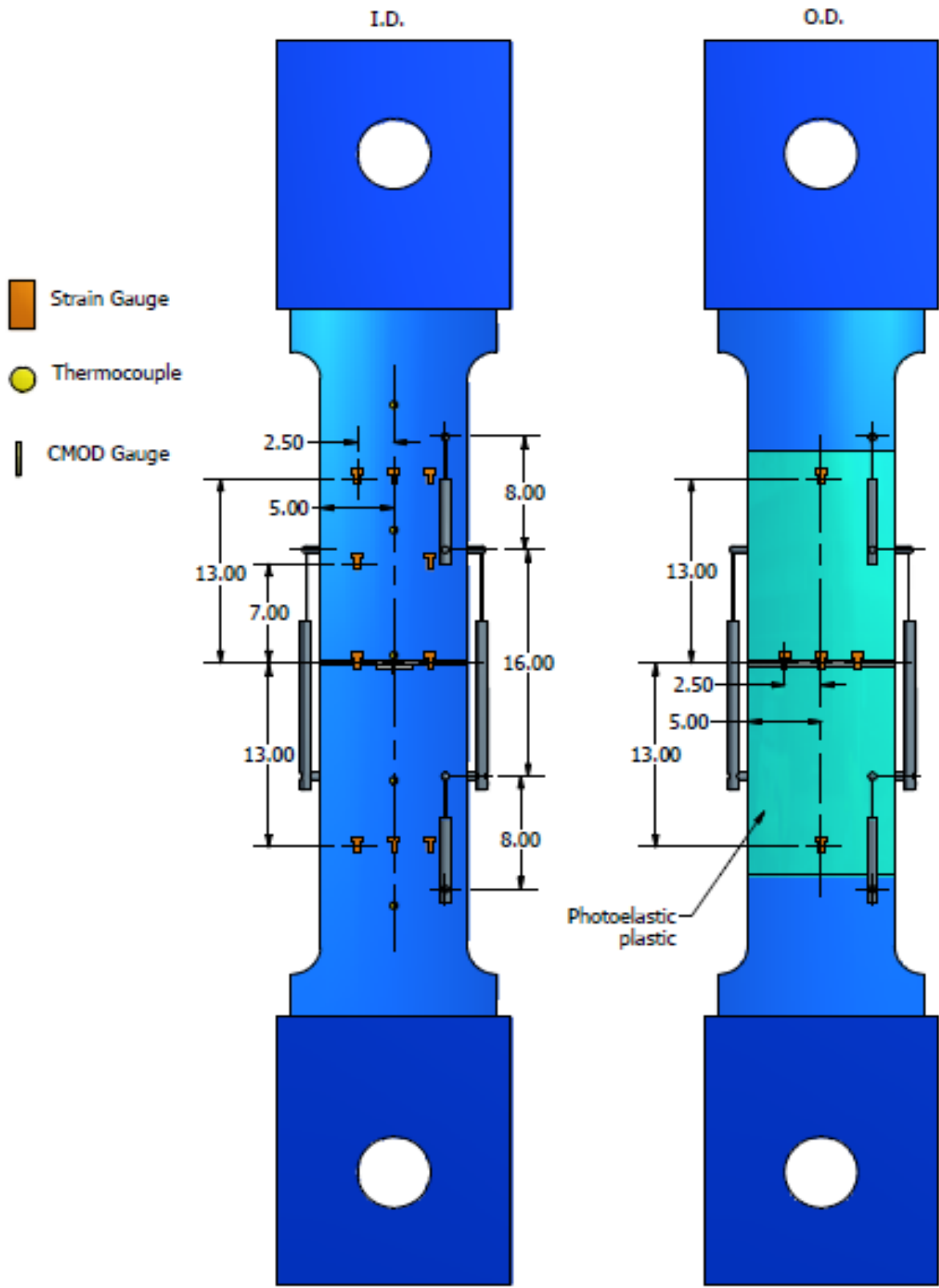


Figure 8: Instrumentation plan of the CWP specimens



**Figure 9: Clip gage arrangement for CMOD measurement**

### **3.3 TEST MATRIX**

The entire test matrix consists of 34 test specimens. The majority of the specimens are from the first round of welding. A smaller number of specimens are from the second round of welding. Four specimens are from the third round of welding. The relevant dimensions and material properties of those welds are covered in other reports of this project.

The entire test matrix is given in Table 1.

Table 1: CWP test matrix

Order of Test	Specimen ID	Round of Welding	Torch Config	Welding Position	Flaw Location	Target Final Flaw Size (mm x mm)	Test Temperature (°C)
1	No ID	1	Pipe Specimen, no weld		BM	3.0 x 50.0	RT
6	No ID	1			BM	3.0 x 50.0	-20
2	CWP-16	1	Single	1G	Weld	3.0 x 50.0	RT
3	CWP-03	1	Single	1G	HAZ	3.0 x 50.0	RT
7	CWP-11	1	Single	1G	Weld	3.0 x 50.0	-20
8	CWP-19	1	Single	1G	Weld	3.0 x 50.0	-20
4	CWP-01	1	Single	1G	Weld	6.0 x 30.0	RT
5	CWP-15	1	Single	1G	HAZ	6.0 x 30.0	RT
9	CWP-10	1	Single	1G	Weld	6.0 x 30.0	-20
10	CWP-12	1	Single	1G	HAZ	6.0 x 30.0	-20
11	CWP-02	1	Single	1G	HAZ	3.0 x 50.0	-20
20	CWP-05	1	Single	1G	HAZ	3.0 x 50.0	-20
22	CWP-06	1	Single	1G	Weld	2.0 x 75.0	RT
21	CWP-07	1	Single	1G	Weld	2.0 x 75.0	-20
23	CWP-08	1	Single	1G	HAZ	2.0 x 75.0	RT
24	CWP-09	1	Single	1G	HAZ	2.0 x 75.0	-20
17	CWP-13	1	Single	1G	Weld	3.0 x 50.0	-40
16	CWP-14	1	Single	1G	Weld	3.0 x 50.0	-40
19	CWP-17	1	Single	1G	HAZ	3.0 x 50.0	-40
18	CWP-18	1	Single	1G	HAZ	3.0 x 50.0	-40
13	CWP-20	2	Dual	1G	Weld	3.0 x 50.0	RT
14	CWP-21	2	Dual	1G	HAZ	3.0 x 50.0	RT
15	CWP-22	2	Dual	1G	Weld	3.0 x 50.0	-20
12	CWP-23	2	Dual	1G	HAZ	3.0 x 50.0	-20
25	CWP-24	2	Dual	1G	Weld	6.0 x 30.0	RT
27	CWP-25	2	Dual	1G	HAZ	6.0 x 30.0	RT
28	CWP-26	2	Dual	1G	Weld	6.0 x 30.0	-20
26	CWP-27	2	Dual	1G	HAZ	6.0 x 30.0	-20
29	CWP-28	2	Dual	1G	Weld	3.0 x 50.0	-40
30	CWP-29	2	Dual	1G	HAZ	3.0 x 50.0	-40
31	CWP-30	3			Weld	2.5 x 50.0	-20
32	CWP-31	3			HAZ	2.5 x 50.0	-20
33	CWP-32	3			HAZ	2.5 x 50.0	-20
34	CWP-33	3			Weld	2.5 x 50.0	-20

## 4 DEVELOPMENT OF COMPLIANCE FUNCTION

### 4.1 INTRODUCTION

One of the overall objectives of this project is to understand the fracture resistance to flaw growth of the X100 welds. The fracture resistance is often represented by resistance curves, which are typically given as a function of the fracture toughness ( $J$  integral or CTOD) versus flaw growth.

A two-step procedure has been established to construct fracture resistance curves from experimental data. In the first step, a compliance function was first developed to calculate the flaw growth from unloading compliance measured in CWP tests. In the second step, a set of  $J$ -correlation equations were established to compute fracture toughness from experimentally measured load vs. CMOD trace. Putting the flaw growth and the fracture toughness together leads to the generation of flaw growth resistance curves.

To establish the relation between CWP unloading compliance and flaw growth, a series of finite element analyses were firstly conducted for CWP specimens with surface-breaking flaws. The results were then organized to obtain the compliance functions for specific specimen geometries.

### 4.2 FINITE ELEMENT MODELS

#### 4.2.1 Geometric Models

A sample finite element model of the CWP specimen is shown in Figure 10. Only half of the specimen was modeled due to symmetry conditions. The weld was modeled at the center of the specimen along the length. The bevel angle was assumed to be 6 degrees. The weld root width was assumed to be 5.0 mm. Flaws were located in either the heat affected zone (HAZ) or the weld metal center line, consistent with experimental test specimens. The full length of the specimen was modeled. The middle section of the model in the length direction is the reduced section. The one-half width and length of the reduced section are  $W$  and  $L$ , respectively. The width and length of the plate shoulders are  $W'$  and  $L'$ , respectively. The radius of the transition region between the reduced section and the plate shoulders is  $R$ . The wall thickness of the specimen is  $t$  and the outside diameter (OD) of the pipe is 36 inches. All the aforementioned geometric dimensions used in the finite element model are consistent with the experimental test specimens and are listed in Table 2.

Table 2: Analysis matrix for compliance function

$R$ (mm)	$2W'$ (mm)	$L'$ (mm)	$2W$ (mm)	$L$ (mm)	$t$ (mm)	$2c$ (mm)	$a$ (mm)
76.2	355.6	76.2	254.0	1016.0	19.1	30.0, 50.0, 75.0	2.0, 4.0, 6.0, 8.0, 10.0, 12.0

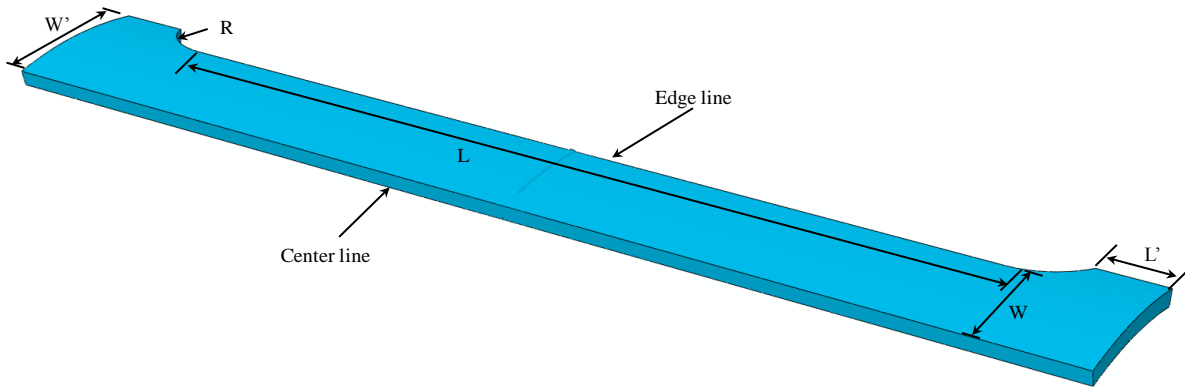


Figure 10: A sample finite element model with relevant dimension designation

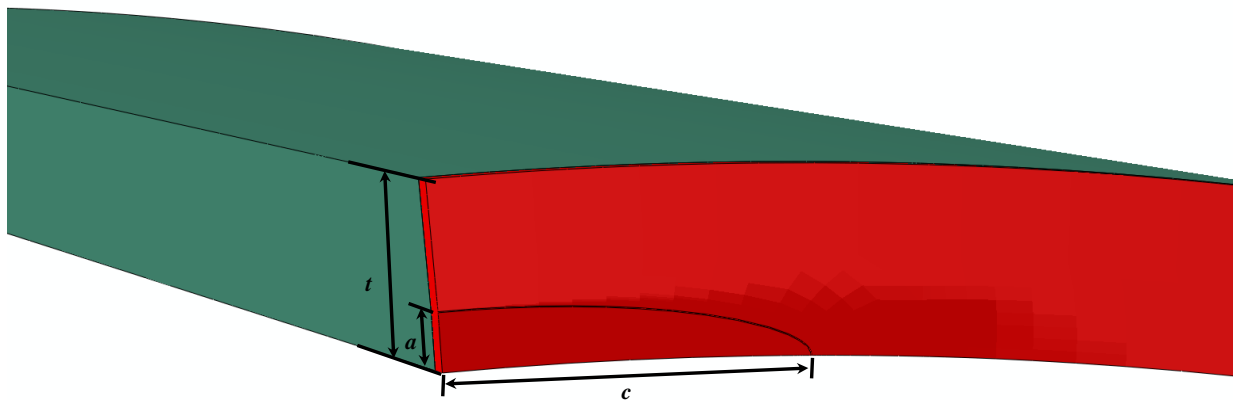


Figure 11: Finite element model in the vicinity of the surface-breaking flaw. The weld metal is shown in red, and the pipe base metal is shown in green

The semi-elliptical shaped flaw is located on the internal diameter (ID) surface of the specimen. It has a surface length of  $2c$  and a depth of  $a$  as shown in Figure 11.

The commercial finite element (FE) software ABAQUS<sup>®</sup> was used to conduct the simulation. Each model contains about 57,000 nodes and 50,000 eight-node 3D elements.

#### 4.2.2 Material Properties

The unloading compliance is a function of the elastic response of the specimen. Therefore, to obtain the relation between unloading compliance and flaw size, only the elastic material properties are needed. The Young's modulus ( $E$ ) is 206.7 GPa and the Poisson's ratio ( $\nu$ ) is 0.3.

#### 4.2.3 Boundary Condition

Symmetry boundary conditions were imposed on the model with respect to the centerline of the CWP, see Figure 10. Longitudinal tension load was imposed by applying a displacement in the length direction at one end of the model while holding the other end fixed. A total of 0.5% engineering strain was applied to the reduced section to determine elastic response.

#### 4.2.4 Data Processing

An important step for establishing the compliance function is the reduction of finite element data. For each CWP model, i.e., one CWP with a surface breaking flaw of specific depth and length, the load and CMOD were directly obtained from the finite element analysis results. Linear regression analysis was then conducted to establish a linear relationship between the load ( $P$ ) and CMOD ( $V$ ), i.e.,  $V=S \cdot P$ , which defines the compliance  $S$ . For the convenience of viewing, a parameter  $M=S \times 10^5$  is used to represent compliance in compliance function.

The calculated compliance was firstly grouped by flaw length  $2c$ . For each flaw length, a second order polynomial interpolation function  $a(M)$  was then developed to calculate flaw depth from compliance as shown in Figure 12. The coefficients of the  $a(M)$  function were further fitted to a set of functions  $A_i(c)$  of crack lengths. Substitution of function  $A_i(c)$  into  $a(M)$  led to the compliance function that uses flaw length and compliance as input and results in flaw depth. In the finite element analysis, the flaw lengths are consistent with those in the X100 CWP experiments and the flaw depth ranges from 2 mm to 12 mm which covers the range from initial flaw depth to expected flaw growth during tests.

### 4.3 RESULTS

Figure 12 shows the compliance-flaw depth relations for the CWP specimens with flaw lengths of 30.0 mm, 50.0 mm and 75.0 mm. It is seen that the relation between the compliance and flaw depth is approximately quadratic ( $2^{\text{nd}}$  order polynomial) for all three flaw lengths. Therefore, quadratic functions were employed to interpolate the relation between flaw depth and compliance. The results indicate that the compliance becomes less sensitive to flaw depth as flaw length decreases. The coefficients ( $A_1$  and  $A_2$ ) of the fitted equations in Figure 12 are summarized in Table 3 where  $A_1$  and  $A_2$  are the coefficient of the  $2^{\text{nd}}$  and  $1^{\text{st}}$  order terms, respectively.

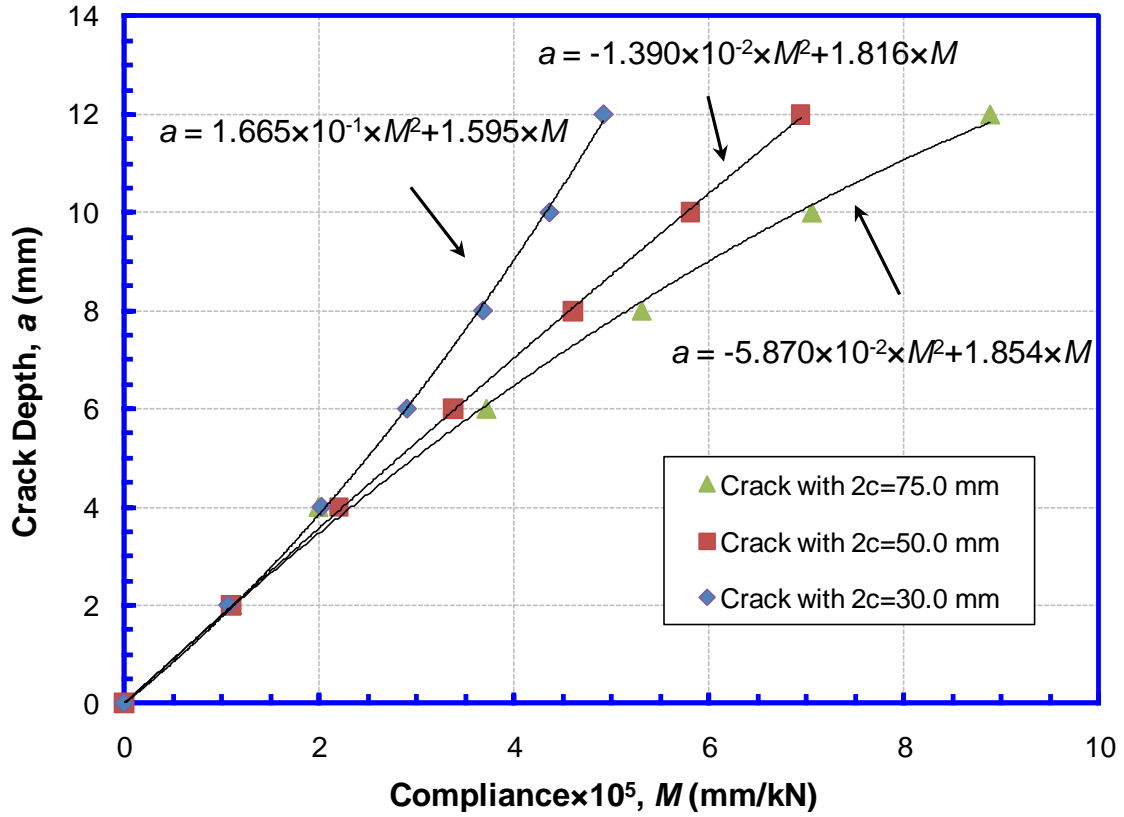


Figure 12: Relation between flaw depth and compliance

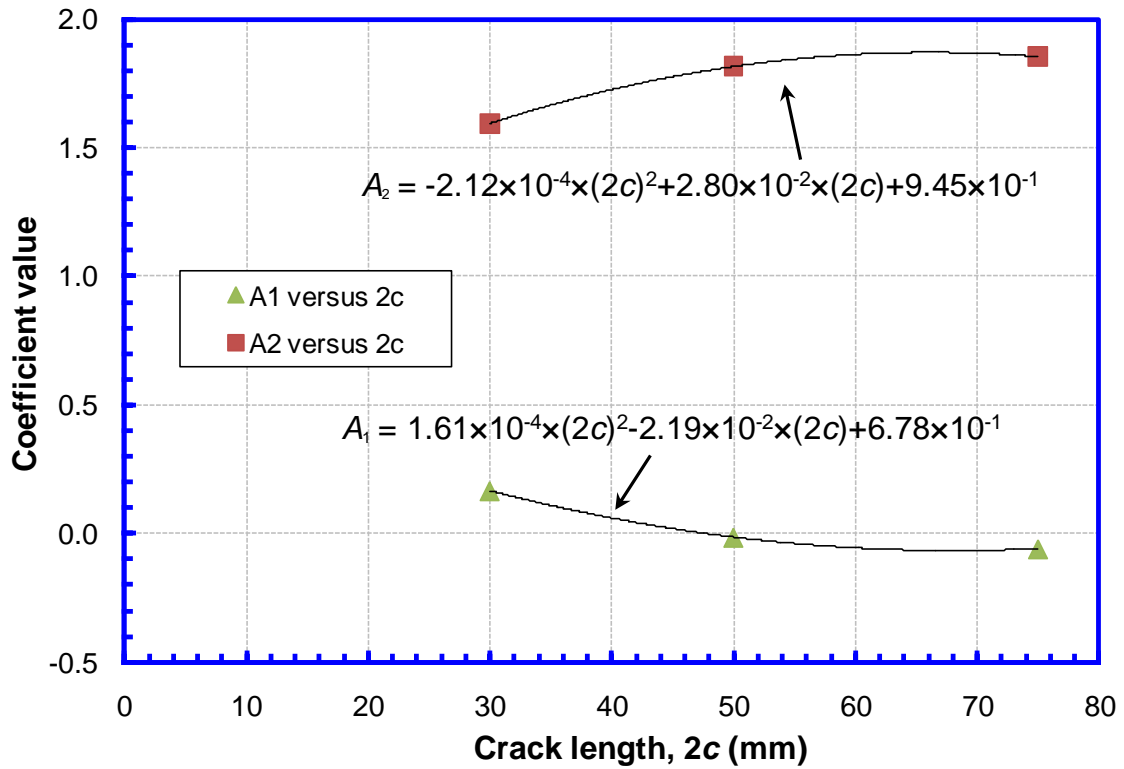


Figure 13: Interpolation coefficients as a function of flaw length ( $2c$ )

The correlation between the coefficients ( $A_1$  and  $A_2$ ) of the fitted equations in Figure 12 and the flaw lengths is plotted in Figure 13. Two parabolic functions were obtained based on the data. The combination of the equations in Figure 12 and Figure 13 leads to the compliance function

$$a = A_1 \times M^2 + A_2 \times M, \quad (1)$$

where

$$A_1 = 1.61 \times 10^{-4} \times (2c)^2 - 2.19 \times 10^{-2} \times 2c + 6.78 \times 10^{-1}, \text{ and} \quad (2)$$

$$A_2 = -2.12 \times 10^{-4} \times (2c)^2 + 2.80 \times 10^{-2} \times 2c + 9.45 \times 10^{-1}. \quad (3)$$

**Table 3: Coefficients of the parabolic functions. A1: coefficient of the 2nd order term, A2: coefficient of the 1st order term**

Crack length (mm)	$A_1$	$A_2$
30.0	$1.67 \times 10^{-1}$	1.59
50.0	$1.39 \times 10^{-2}$	1.82
75.0	$-5.87 \times 10^{-2}$	1.85

#### 4.4 DISCUSSION

The compliance function provides a convenient method for the calculation of flaw depth. It allows a quick and direct estimation of flaw depth from CMOD vs. load trace measured in CWP tests. Given the flaw depth and length used in the finite element analysis (as listed in Table 4), the applicable ranges of the compliance function are 0.0 to 12.0 mm for flaw depth and 30.0 to 75.0 mm for flaw length.

## 5 DEVELOPMENT OF *J*-CORRELATION EQUATIONS

### 5.1 INTRODUCTION

This section covers the development of *J*-correlation equations to estimate fracture toughness. A series of finite element analyses were firstly conducted on the CWP with surface-breaking flaws of different lengths and depths. Data processing and interpolation were performed to obtain the *J*-correlation equations as functions of geometric parameters.

### 5.2 FINITE ELEMENT MODELS

#### 5.2.1 Geometric Models

The overall dimensions of the CWP are the same as those of the model described in Section 4. The flaw dimensions in the finite element analysis are listed in Table 4. The commercial finite element (FE) software ABAQUS<sup>®</sup> was used to conduct the simulation. Similar to the size of the finite element model used in Chapter 4, there were approximately 57,000 nodes and 50,000 eight-node 3D elements in the current model.

**Table 4: Analysis geometry matrix for J-correlation equations**

Geometry	
2c (mm)	a (mm)
30.0, 50.0, 75.0	2.0, 3.0, 4.0, 5.0, 6.0, 7.0, 8.0, 9.0, 10.0

### 5.2.2 Material Properties

Three different grades of steels, X65, X80 and X100, were studied. Their yield strengths (YS) and ultimate tensile strengths (UTS) were obtained as the median values of the range from API Specification 5L/ISO 3183. The CSAZ662 equation was employed to construct the stress-strain curve for finite element analysis, i.e.

$$\varepsilon = \frac{\sigma}{E} + \left(0.005 - \frac{\sigma_y}{E}\right) \left(\frac{\sigma}{\sigma_y}\right)^n \quad (4)$$

where  $\sigma$  is engineering stress,  $\varepsilon$  is engineering strain,  $\sigma_y$  is the yield strength and the strain hardening exponent ( $n$ ) was calculated from the equation

$$n = \frac{3.14}{1 - Y/T} \quad (5)$$

Here  $Y/T$  is the ratio of yield strength over ultimate tensile strength (UTS). All the material properties used in the finite element analysis are listed in Table 5.

### 5.2.3 Boundary Condition

The boundary conditions applied are similar to those used in Section 4. Symmetric boundary conditions were imposed at the centerline of CWP. One end of the model was held fixed and a displacement was applied at the other end. For the longitudinal tension load, a total of 5.0% engineering strain was applied to the reduced section.

**Table 5: Material property matrix for development of J-correlation equations**

Material Properties			
Steel Class	YS (MPa)	UTS (MPa)	Strain Hardening Exponent ( $n$ )
X65	525.0	647.5	16.6
X80	630.0	725.0	24.0
X100	765.0	875.0	27.0

### 5.2.4 Data Processing

The finite element analysis results were firstly processed in developing an  $\eta$  (see definition below) factor equation for CWP. The  $J$  integral, CMOD and load were obtained from the finite element results. The  $J$  integral was calculated at the center plane, i.e., at the mid-length in the

flaw length direction. The flaw growth was expected to be the greatest at this location. The CMOD value at the mid-length was also used.

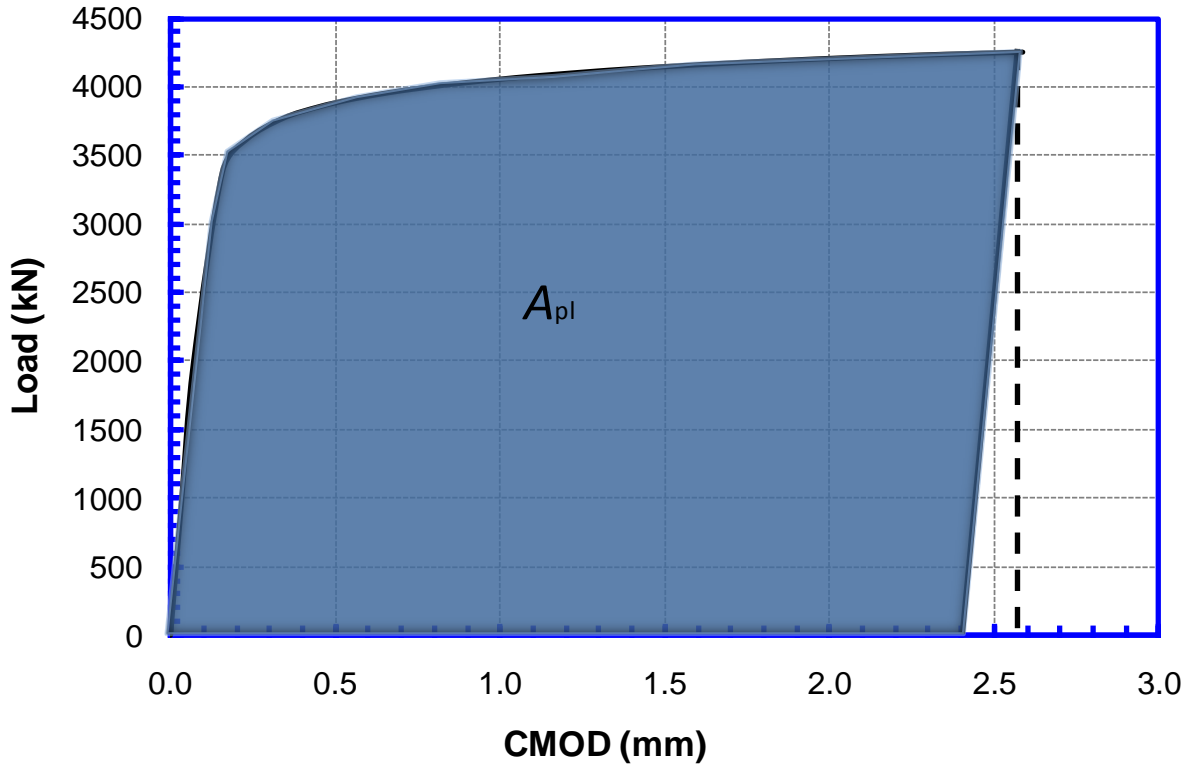


Figure 14: Definition of the plastic component of the area under the load versus CMOD curve

A general  $J$  integral estimation approach based on CMOD was adopted in the data processing procedure. The advantage of using CMOD rather than the overall displacement of the specimen is that CMOD provides more direct measure of the crack tip deformation. The total value of  $J$  integral is partitioned into a small scale yielding and a fully plastic part, consistent with established practice and standards, such as ASTM E1820 [15,16]. The small scale yielding component is defined as a function of stress intensity factor  $K$  and the fully plastic  $J$  integral is calculated from the plastic component of the area ( $A_{pl}$ ) under load-CMOD curve, which, as described in Figure 14, is the integral of the load versus CMOD less the elastic component.

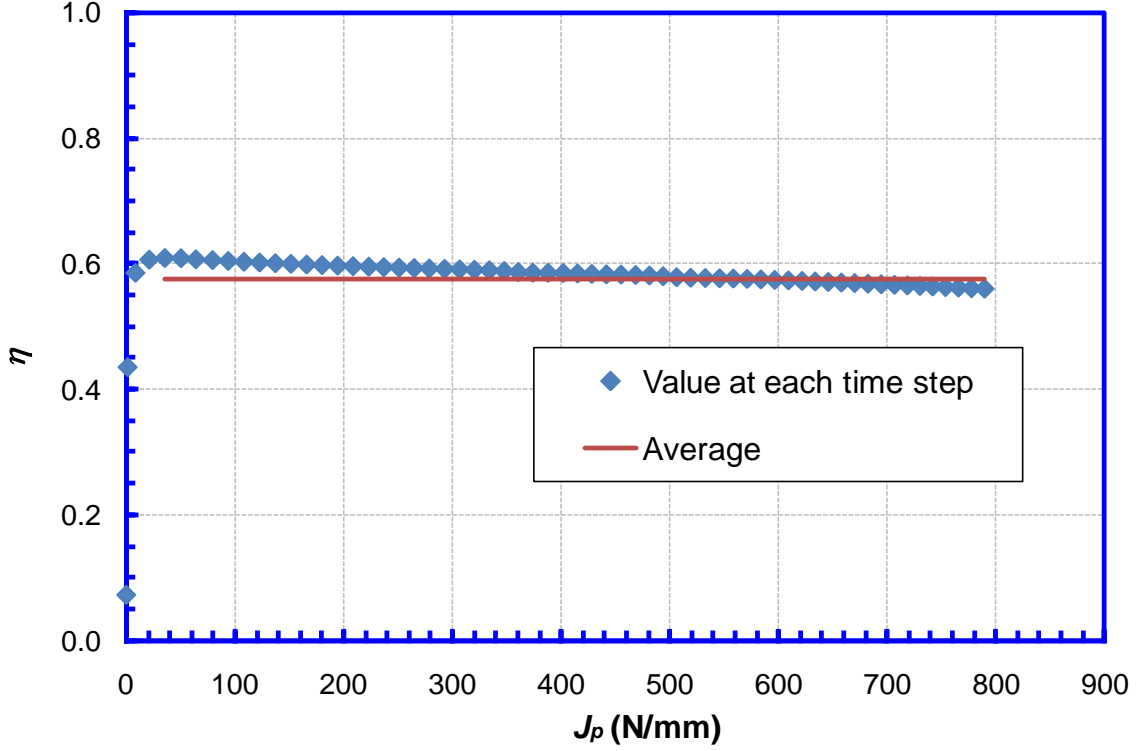


Figure 15: Schematic description of  $\eta$  factor evaluation

The  $J$  estimation formula has the following form:

$$J = J_e + J_p \quad (6)$$

where  $J_e$  is the elastic component and  $J_p$  is the plastic component. These can be derived/computed as

$$J_e = \frac{K^2(1-\nu^2)}{E} \quad (7)$$

and

$$J_p = \frac{\eta A_{pl}}{W(t-a)} \quad (8)$$

where  $\eta$  is a non-dimensional factor. Derivation from Equation (6) and Equation (8) leads to

$$\eta = \frac{(J - J_e) W(t-a)}{A_{pl}} \quad (9)$$

A closed form solution of stress-intensity factor  $K$  for a surface-breaking flaw in a flat plate under tension given in ASTM E740-03, Annex A2 [17] was used to compute the elastic  $J$ . Under an uniform tensile stress  $\sigma$  at the deepest point (mid-length along the flaw length direction), the stress intensity factor is given as,

$$K = \sigma \sqrt{\pi a} M / \Phi, \quad (10)$$

where

$$M = \{1.13 - 0.09(a/c)\} + \{-0.54 + 0.89[0.2 + (a/c)]^{-1}\}(a/t)^2 + \{0.5 - [0.65 + (a/c)]^{-1} + 14(1 - a/c)^{24}\}(a/t)^4 \quad (11)$$

and

$$\Phi^2 = 1 + 1.464(a/c)^{1.65}. \quad (12)$$

For each finite element CWP model, the plastic component of the area ( $A_{pl}$ ) at any load step was evaluated by the method shown in Figure 14. The evaluation of  $\eta$  factor is described by Figure 15. At each load step, the value of  $J$  was taken at the point of deepest crack depth (mid-length of the crack) from the contour integral around the tip of crack. The  $\eta$  factor was determined from Equation (9) and was plotted versus  $J_p$ . The first few data points at the initial loading were not used to compute  $\eta$  as they reflect non-stabilized values before the material behavior becomes fully plastic. With the increase of  $J_p$ , the  $\eta$  factor becomes constant as shown in Figure 15. The averaged value over the stable range was taken as the  $\eta$  factor for a specific model.

A total of 81 cases were analyzed as shown in Table 5. Among these cases, the maximum ratio  $2c/W$  was 75/254 which is less than 1/3. It was assumed that the boundary effect at the edge lines would not affect the stress fields around the flaw. A series of curve fittings were conducted based on the results of  $\eta$  factors and the corresponding normalized crack geometry factors  $a/t$ ,  $2c/t$  and material properties  $n$  to develop an equation for  $\eta$  factor. Both the finite element results and curve fittings indicated that the  $\eta$  factor was almost independent of strain hardening exponent ( $n$ ). In other words, the  $\eta$  factor is only dependent on the normalized crack geometry factors  $a/t$ ,  $2c/t$ .

### 5.3 RESULTS

According to previous discussion, the final equation of  $\eta$  factor depends only on the normalized crack geometry and was derived as

$$\eta = -1.821(a/t)^2 + 0.119(a/t) + 0.427 + 0.195\{\ln[1 + 8.064(2c/t)]\}^{0.5} \quad (13)$$

After the development of the  $\eta$  factor equation, the  $J$  integral was computed from load and CMOD data. It should be noted that Equation (8) only calculates the plastic component of  $J$  integral with an assumption that the initial flaw size remains stable and without growth. In the context of generating resistance curves from experimental tests, the flaw depth is a variable. The depth increases with the increase of applied load/displacement. Consequently the area under load vs. CMOD trace has to be updated with current flaw depth. A set of incremental form of equations from ASTM E1820 is adopted for the calculation of  $J$ -integral that accounts for flaw growth. The incremental equation for the plastic component of  $J$  integral is given as

$$J_{p(i)} = \left( J_{p(i-1)} + \frac{\eta_{i-1}}{W(t-a_{i-1})} A_{pl}^{i-1,i} \right) \left[ 1 - \frac{\gamma_{i-1}}{(t-a_{i-1})} (a_i - a_{i-1}) \right], \quad (14)$$

where  $\eta_{i-1}$  is calculated from Equation (13) as a function of  $a_{i-1}$  while keeping  $2c$  and  $t$  as constants. The parameter  $A_{pl}^{i-1,i}$  is the increment of the plastic area under the load-CMOD curve from step  $i-1$  to  $i$ , i.e.,

$$A_{pl}^{i-1,i} = 0.5(P_i + P_{i-1})(V_{p(i)} - V_{p(i-1)}), \quad (15)$$

where  $P_i$  is the load at step  $i$ ,  $V_{p(i)}$  is the plastic component of CMOD at step  $i$ . The parameter  $V_p$  is given as  $V - V_e$ , where  $V_e$  can be calculated as load times the elastic unloading compliance.

In the second bracket of Equation (14), the last term including  $\gamma_{(i-1)}$  is geometric correction which considers the influence of crack growth. In CWP tests, as the cracked area is very small in comparison with the overall specimen cross section, the influence of the crack growth on  $J$  is small and Equation (14) reduces to

$$J_{p(i)} = \left( J_{p(i-1)} + \frac{\eta_{i-1}}{W(t-a_{i-1})} A_{pl}^{i-1,i} \right) \quad (16)$$

with acceptable accuracy, setting the term in square brackets in Equation (14) equal to unity.

A set of  $J$ -correlation equations was developed by substituting the  $\eta$  factor, Equation (13), into Equations (14-16). These equations use load and CMOD as inputs for the computation of  $J$ -integral for specimens with specific  $2c/t$  ratios.

## 5.4 DISCUSSION

A set of  $J$  correlation equations for the evaluation of  $J$ -integral from the CWP tests have been developed. The key component of the  $J$  correlation equations is the  $\eta$  factor, i.e., Equation (13). When the flaw length is small in comparison to the wide plate width (e.g., flaw length less than 1/5 of the wide plate width) and the boundary effects from the finite plate width is minimal, the  $\eta$  factor solution can be applied to CWP of a range of width. Given the thickness of CWP specimen used in the finite element analysis and the flaw dimensions listed in Table 4, the applicable ranges of the  $J$  correlation equations are  $a/t$  of 0.2 to 0.5 and  $2c/t$  of 1.6 to 3.9. A wide range of applicability is possible, but such range needs to be verified.

## 6 EXAMINATION OF TEST RESULTS

### 6.1 INTRODUCTION

A uniform data processing and presentation format is used for all CWP test data. The data from each test are presented in a Microsoft Excel<sup>®</sup> file. The data are organized as:

- 1) Summary of specimen and test information,
- 2) Specimen dimensions and test setup,
- 3) Raw data and processed data, and
- 4) Presentation of the processed data in plot formats.

Data is plotted in a total of 19 graphs to illustrate relations among a variety of variables. The relevant variables for each graph are given in Table 6.

**Table 6: Description of the data graphs**

No.	X-axis	Y-axis 1	Y-axis 2
1	Ram Displacement	Load	CMOD
2	Ram Displacement	Applied Stress	
3	Ram Displacement	Remote Strains above Weld (1A, 2A and AVE)	
4	Ram Displacement	Remote Strains below Weld (1B, 2B and AVE)	
5	Ram Displacement	Strain across Weld	
6	Average Remote Strain below Weld	Average Remote Strain above Weld	
7	CMOD	Average Strains above and below Weld	
8	CMOD	Average Strain across Weld	
9	CMOD	Compliance	
10	Average Remote Strain above Weld	Compliance	
11	Average Remote Strain below Weld	Compliance	
12	Flaw Depth	CMOD	
13	Strain	Flaw Depth	
14	Average Remote Strain above Weld	Stress above Weld	
15	Average Remote Strain below Weld	Stress below Weld	
16	Average Remote Strain above Weld	CMOD	
17	Average Remote Strain below Weld	CMOD	
18	Flaw Growth ( $\Delta a$ )	J	
19	CMOD	Applied Stress	

## 6.2 SAMPLE TEST DATA

To illustrate the standard data presentation format, the results of CWP-11 are presented in detail in this section. The specimen has a surface-breaking semi-elliptical flaw of 3 mm  $\times$  50 mm (depth  $\times$  total surface length) in the weld centerline and was tested at -20°C.

### 6.2.1 Load and CMOD vs. Cross-Head Displacement

Figure 16 shows load and CMOD as functions of cross-head displacement. Both data records are directly read from the experimental data. There is a dramatic increase in CMOD after the CMOD reaches approximately 1.6 mm.

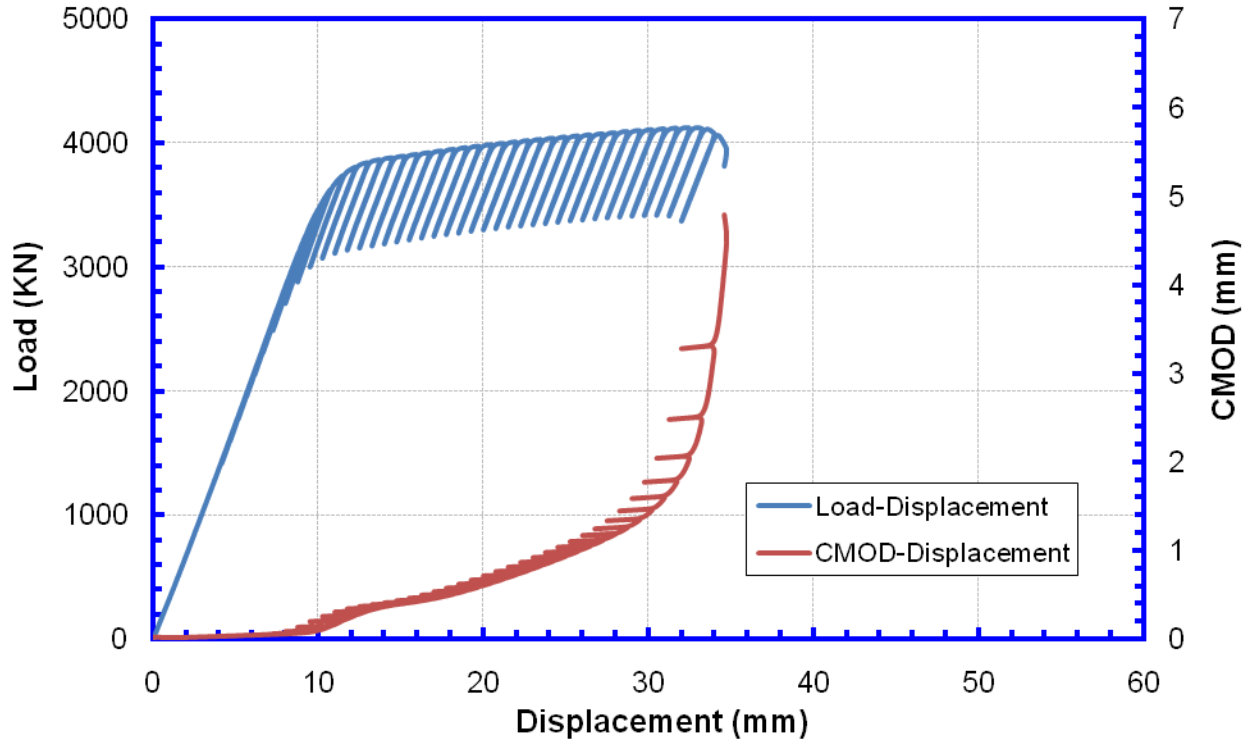


Figure 16: Load-displacement and CMOD-displacement relation of CWP-11

### 6.2.2 Stress vs. Cross-Head Displacement

The stress above or below the weld was calculated by dividing the measured load by the cross-sectional area of the reduced section of the CWP. The cross section was calculated from the measured chord length ( $L_c$ ), wall thickness ( $t$ ) and outer diameter ( $D$ ). As shown in Figure 17, the angle  $\theta$  was calculated from chord length ( $L_c$ ) and outer radius ( $R=0.5 \times D$ ) as

$$\theta = 2 \cdot \sin^{-1}(0.5 \cdot L_c / R). \quad (17)$$

The CWP cross section area bounded by the dashed line is

$$S_1 = \frac{\theta}{2} \cdot [(R)^2 - (R-t)^2], \quad (18)$$

and the area beyond the dashed lines, or the areas of the two corners at the left and right hand side of the CWP, is

$$S_2 = \frac{t}{2} \cdot [R \cdot \theta - (R-t) \cdot \theta] \quad (19)$$

Therefore, the cross section area is

$$S = S_1 + S_2 \quad (20)$$

The stress as a function of the displacement is given in Figure 18. There was no difference in the cross-sectional area above and below the weld. Therefore the stresses at locations above and below the weld are the same.

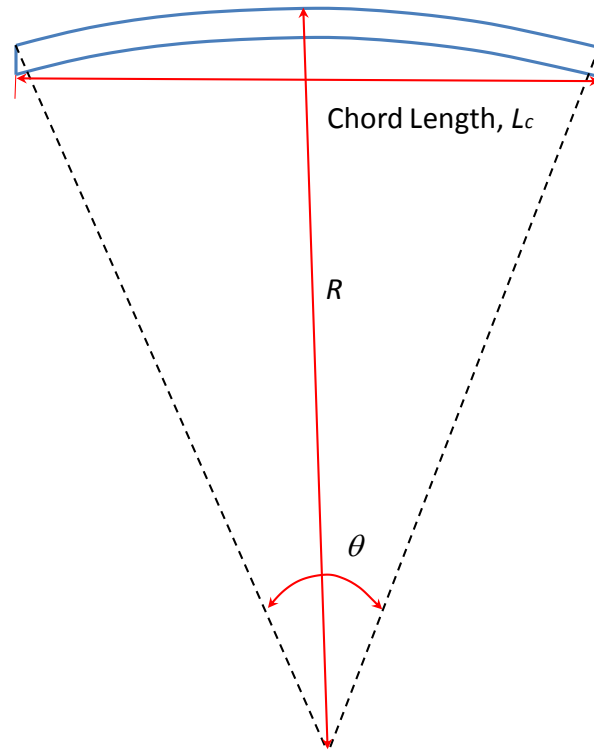


Figure 17: Description of the cross section area calculation

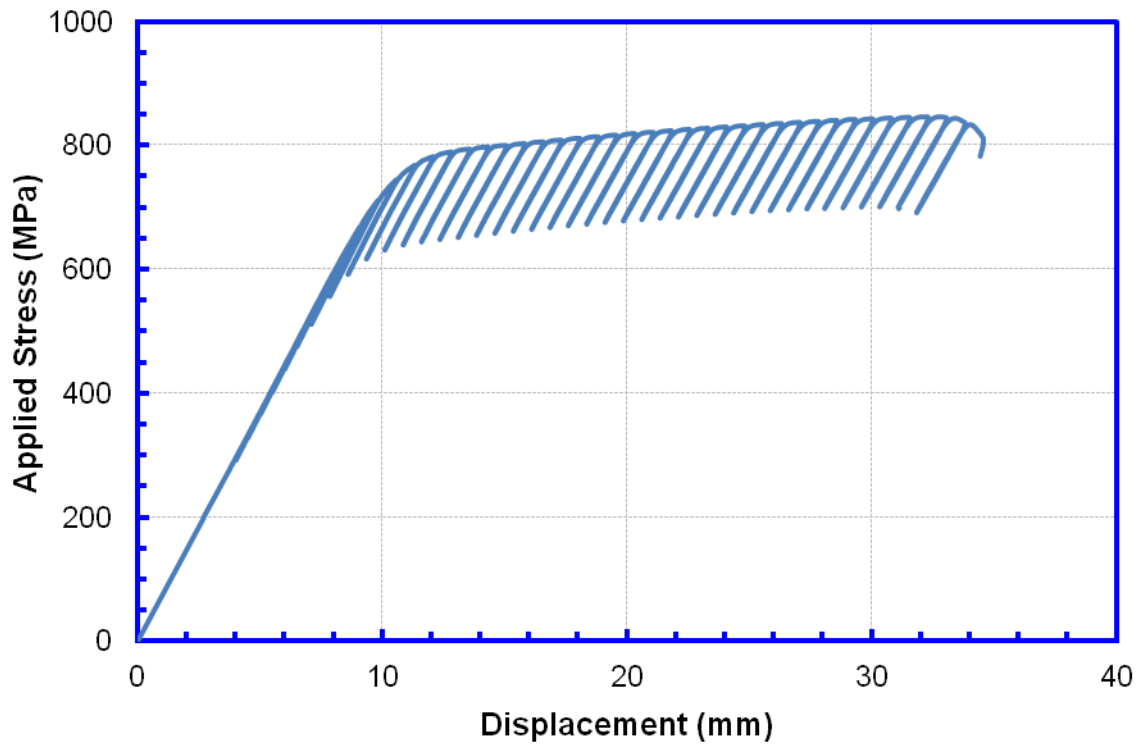


Figure 18: Stress and displacement relation of CWP-11

### 6.2.3 Remote Strain vs. Displacement

The strains measured respectively from above the weld, below the weld and across the weld of both the inner diameter and outer diameter side and the corresponding averages are shown in Figure 19, Figure 20 and Figure 21.

The remote strains above or below the weld are calculated by dividing the corresponding LVDT displacements by the original gage length of the LVDT. In Figure 19 and Figure 20, LVDTs 1A and 1B give the displacement on the ID side and LVDTs 2A and 2B give the displacement on the OD side. The average strain is the mathematical average of the strains from ID and OD sides.

### 6.2.4 Average Strain above and below Weld

Figure 22 shows the average strain below the weld versus that above the weld. The strain in the pipe above the weld is higher than the strain below the weld.

### 6.2.5 Strain vs. CMOD

Figure 23 shows the strain above and below the weld vs. the CMOD. Figure 24 shows the average strain measured by the LVDTs straddling the weld vs. the CMOD. When the CMOD is less than 2 mm, the remote strain is greater than the average strain across the weld. When the CMOD passes beyond 2 mm, the strains in the remote region reach a plateau, while the strain straddling the weld continues to increase. The increase of the average strain from the LVDTs straddling the weld correlates with growth of the CMOD without increase of load, as shown in Figure 16.

### 6.2.6 Compliance vs. CMOD

The unloading compliances were calculated from the experimentally measured CMOD and load data. Figure 25 shows the load history vs. CMOD. The specimen underwent loading and unloading during the test. The unloading relation between CMOD ( $V$ ) and load ( $P$ ) is nearly linear. Linear regression analysis was performed on each unloading load-CMOD curve to determine the compliance  $S$  by the relationship  $V=S \times P$ . For each unloading process, both unloading and reloading data in the range between the point marked by green dots and the end point of current unloading marked by red dots were used to calculate the compliance. Table 7 lists the compliance of each unloading cycle. CMOD values were measured at the start points of the unloading processes which are marked as red circles in Figure 25.

The compliance versus CMOD relation is plotted in Figure 26.

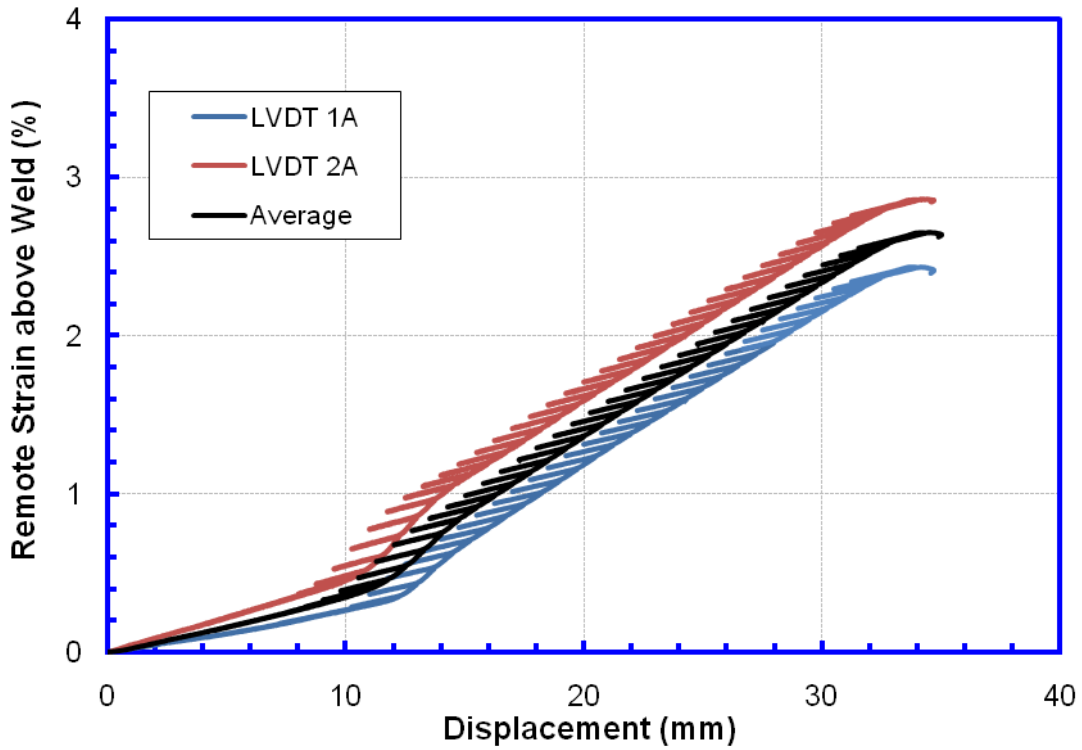


Figure 19: Remote strain versus displacement above the weld of CWP-11

#### 6.2.7 Compliance versus Average Strain

Table 7 also lists average strain values at the start points of the unloading processes from LVDTs above and below the weld. The relations between compliance and average strains at locations above and below the weld of CWP-11 were also demonstrated in Figure 27 and Figure 28, respectively.

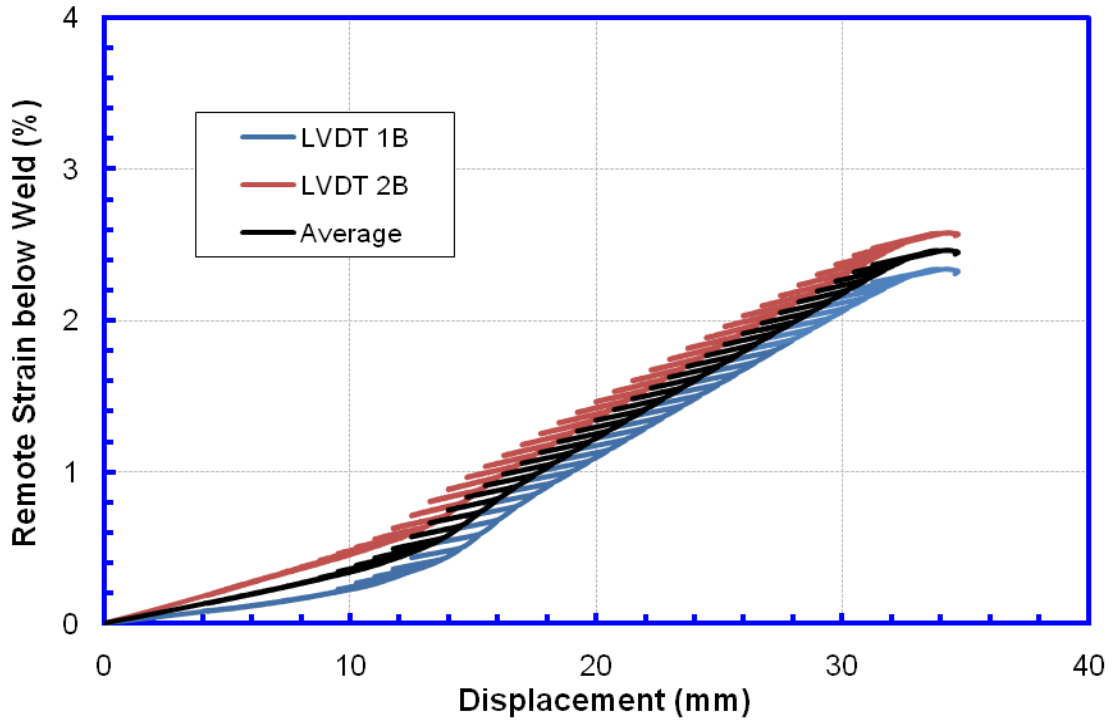


Figure 20: Remote strain versus displacement below the weld of CWP-11

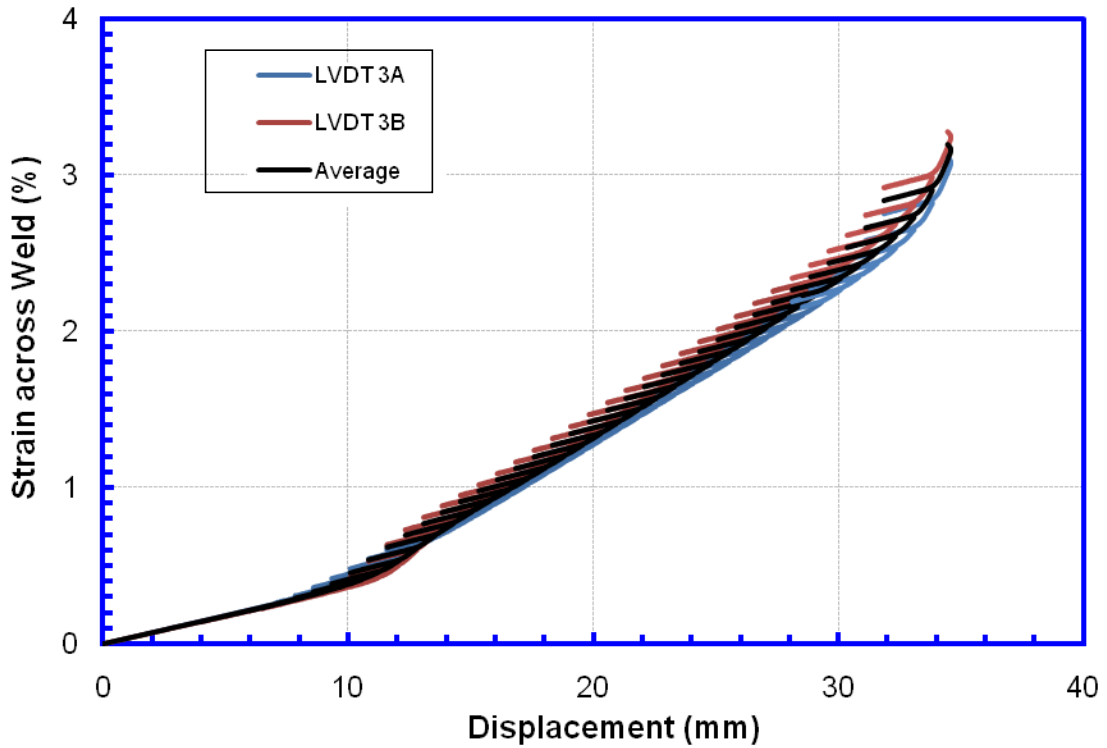


Figure 21: Strain across the weld versus displacement of CWP-11

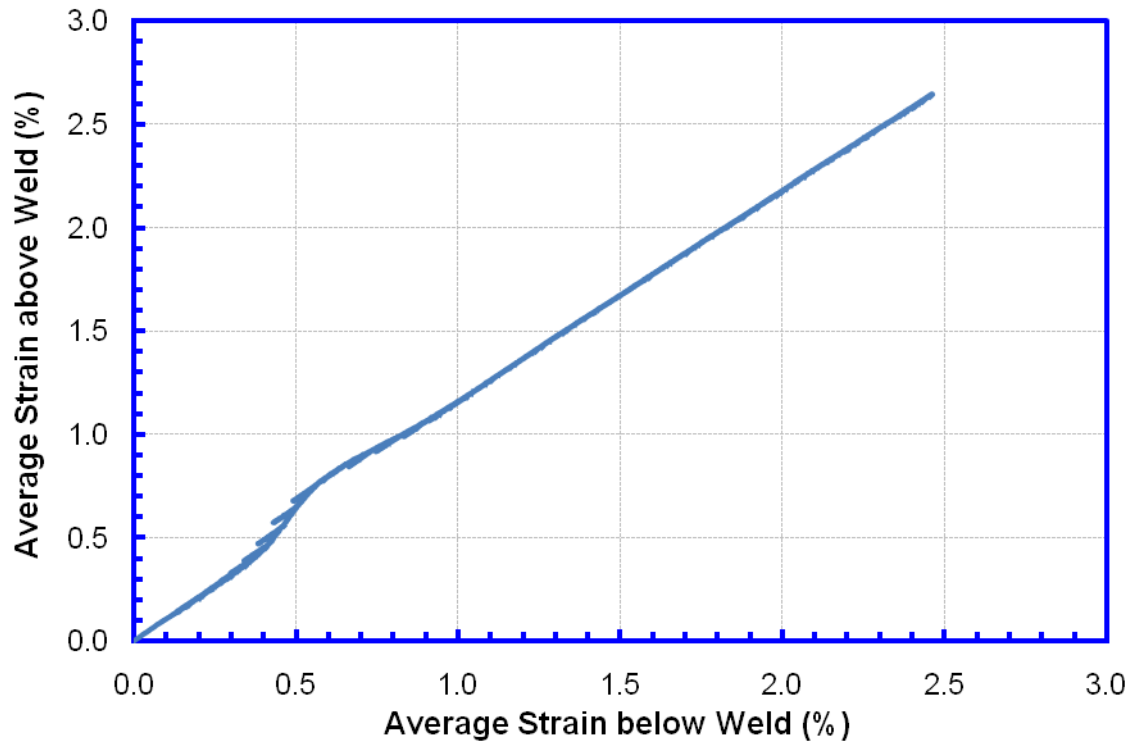


Figure 22: Average strain above the weld versus average strain below the weld of CWP-11

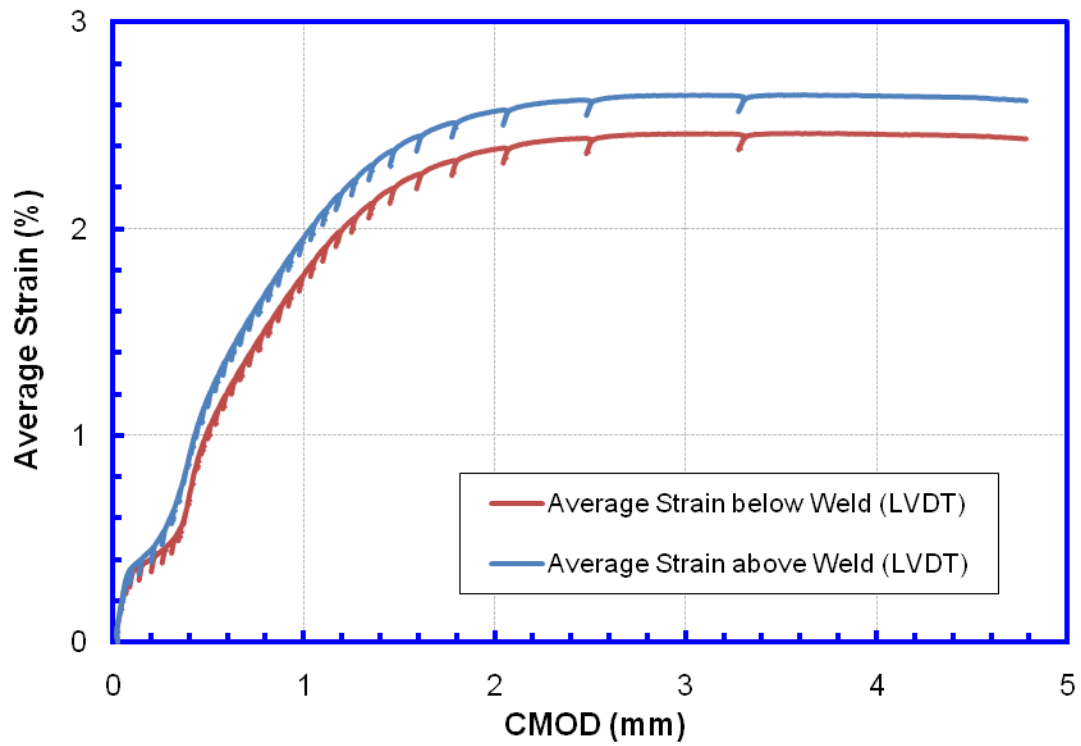


Figure 23: Average strain above and below the weld of CWP-11 versus CMOD

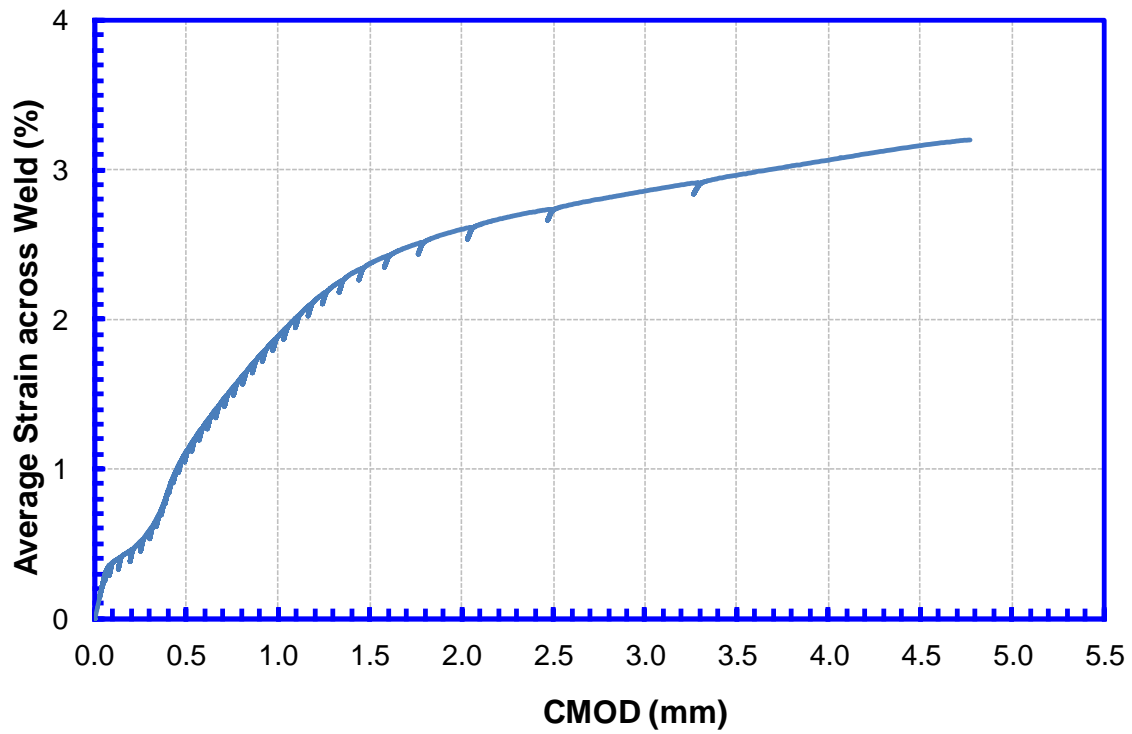


Figure 24: Average strain across the weld versus CMOD of CWP-11

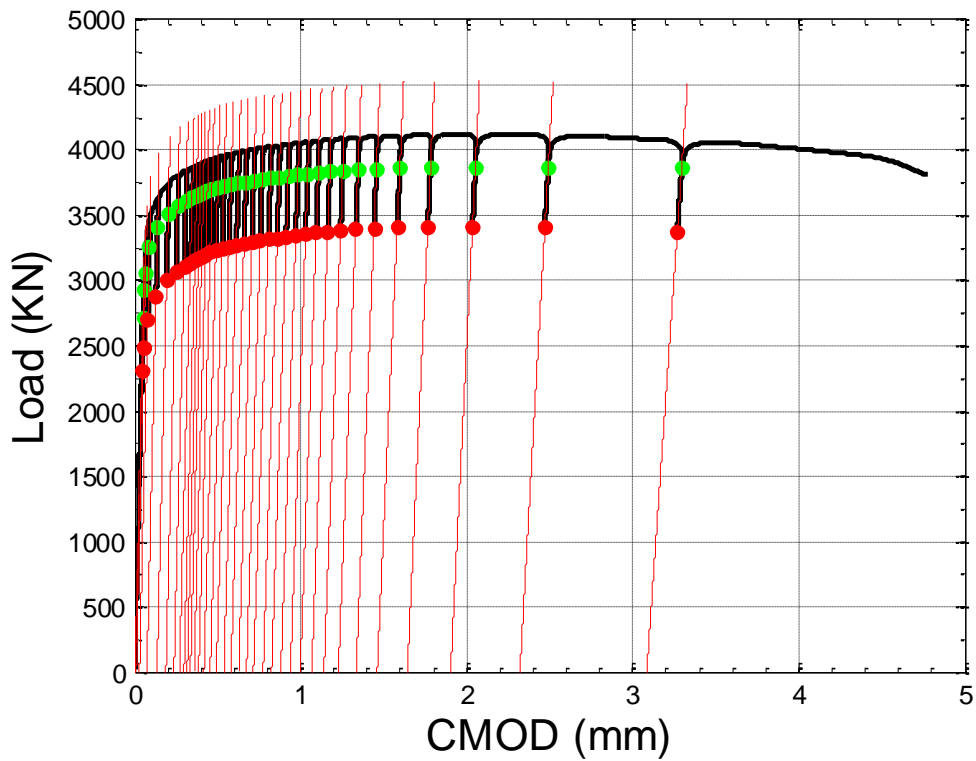


Figure 25: Load-CMOD plot for specimen CWP-11

**Table 7: CWP-11 response as measured by various parameters as a function of the unloading sequence**

No. of Unloading Sequence	Compliance	CMOD	Average Strain above Weld (LVDT)	Average Strain below Weld (LVDT)	Average of Remote Strains above and below Weld	Average strain across weld	Flaw Depth
	(mm/kN)	(mm)	(%)	(%)	(%)	(%)	(mm)
1	1.78E-05	0.05	0.26	0.25	0.26	0.27	3.19
2	1.78E-05	0.05	0.28	0.27	0.28	0.29	3.19
3	1.77E-05	0.06	0.31	0.30	0.30	0.32	3.16
4	1.81E-05	0.06	0.33	0.31	0.32	0.34	3.24
5	1.84E-05	0.09	0.36	0.34	0.35	0.37	3.30
6	1.88E-05	0.14	0.40	0.37	0.39	0.41	3.36
7	1.92E-05	0.20	0.46	0.41	0.44	0.46	3.43
8	1.99E-05	0.26	0.54	0.45	0.50	0.53	3.56
9	2.01E-05	0.31	0.64	0.50	0.57	0.61	3.59
10	2.09E-05	0.35	0.74	0.56	0.65	0.69	3.73
11	2.06E-05	0.37	0.83	0.64	0.73	0.77	3.67
12	2.08E-05	0.39	0.91	0.72	0.82	0.84	3.72
13	2.10E-05	0.41	0.99	0.82	0.90	0.92	3.75
14	2.16E-05	0.44	1.06	0.90	0.98	0.98	3.86
15	2.19E-05	0.47	1.13	0.98	1.05	1.05	3.91
16	2.23E-05	0.50	1.20	1.05	1.12	1.12	3.98
17	2.24E-05	0.54	1.28	1.13	1.21	1.20	4.00
18	2.36E-05	0.58	1.35	1.19	1.27	1.26	4.19
19	2.32E-05	0.62	1.43	1.26	1.35	1.34	4.14
20	2.41E-05	0.67	1.50	1.34	1.42	1.42	4.28
21	2.42E-05	0.72	1.57	1.40	1.48	1.48	4.30
22	2.47E-05	0.77	1.64	1.47	1.55	1.55	4.40
23	2.74E-05	0.82	1.72	1.55	1.64	1.64	4.86
24	2.55E-05	0.87	1.79	1.62	1.70	1.71	4.54
25	2.64E-05	0.92	1.86	1.69	1.77	1.78	4.69
26	2.67E-05	0.98	1.94	1.76	1.85	1.86	4.75
27	2.71E-05	1.04	2.00	1.83	1.91	1.93	4.81
28	2.84E-05	1.11	2.08	1.91	2.00	2.02	5.04
29	2.84E-05	1.18	2.15	1.98	2.06	2.09	5.03
30	2.96E-05	1.25	2.23	2.05	2.14	2.17	5.25
31	3.07E-05	1.35	2.30	2.12	2.21	2.25	5.44
32	3.17E-05	1.46	2.37	2.20	2.29	2.33	5.62
33	3.54E-05	1.60	2.44	2.26	2.35	2.41	6.25
34	3.59E-05	1.78	2.50	2.32	2.41	2.49	6.33
35	3.85E-05	2.05	2.56	2.38	2.47	2.58	6.78
36	4.41E-05	2.49	2.62	2.44	2.53	2.72	7.73
37	5.44E-05	3.29	2.64	2.46	2.55	2.78	9.45

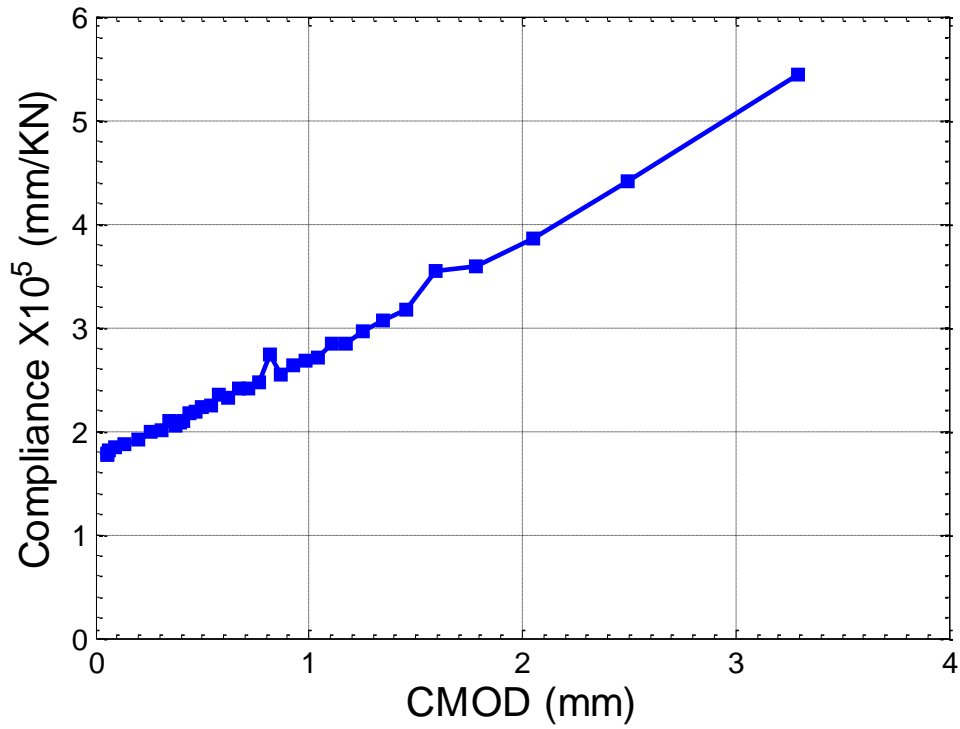


Figure 26: Compliance versus CMOD of CWP-11

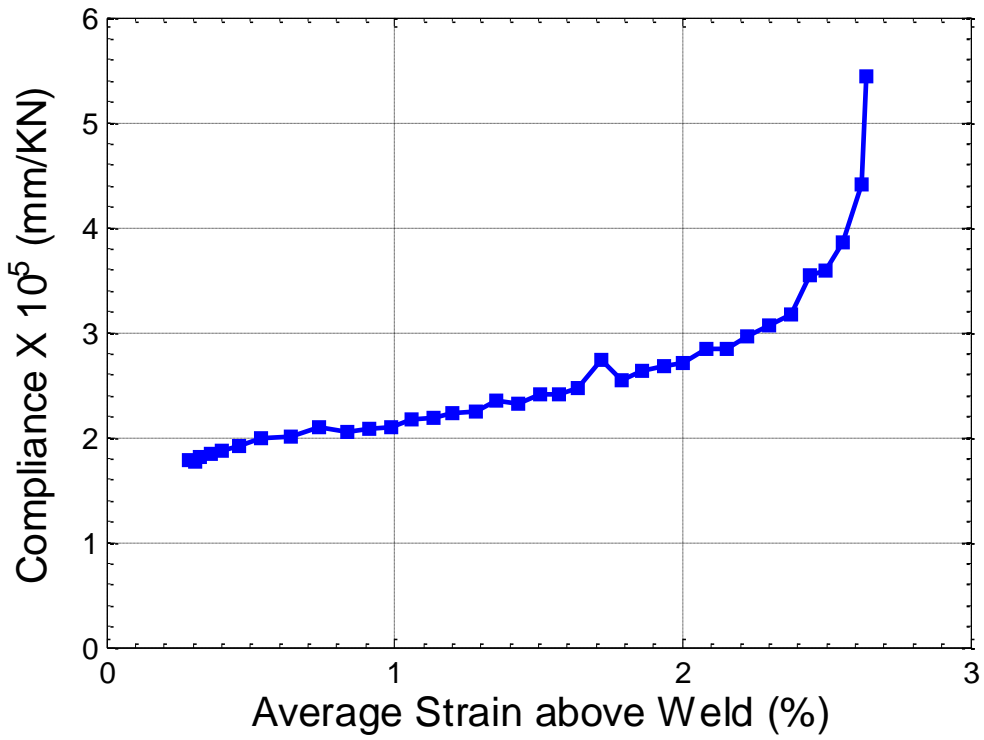


Figure 27: Compliance versus average strain above the weld of CWP-11

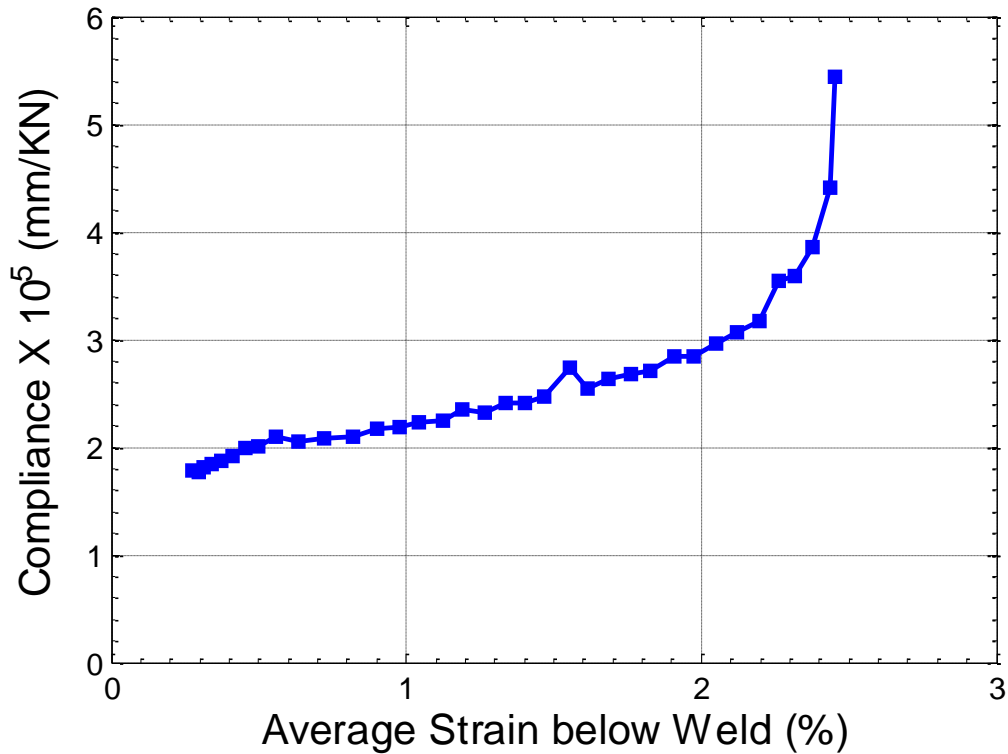


Figure 28: Compliance versus average strain below weld of CWP-11

#### 6.2.8 CMOD vs. Flaw Depth

Specimen CWP-11 contained a surface-breaking flaw with nominal initial size  $a \times 2c = 3 \times 50$  mm. Given the compliances in Table 7 as input, Equation (1) in Section 4 was used to evaluate flaw depth which is also listed in Table 7. The predicted flaw depth is related to the experimentally measured CMOD value in Figure 29.

#### 6.2.9 Flaw Depth vs. Strains

Table 7 lists the average of remote strain values above and below the weld and the averaged strain values from LVDTs across the weld. The relations between flaw depth and those two strain measures are shown in Figure 30.

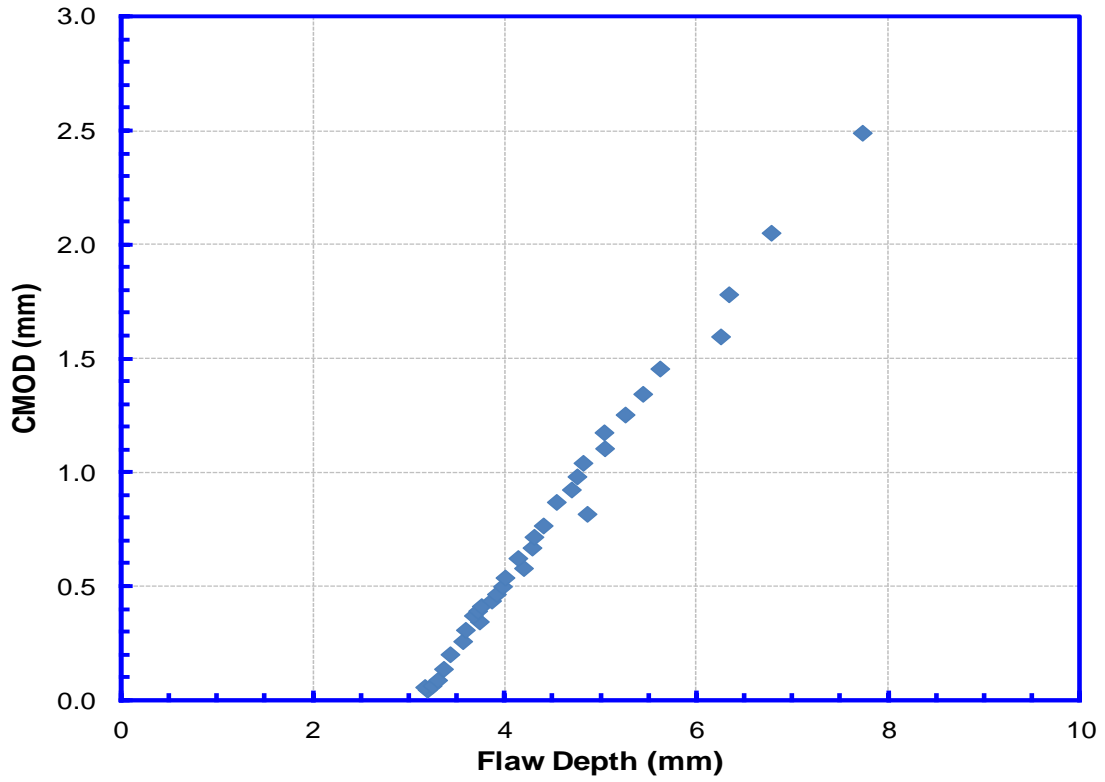


Figure 29: CMOD and flaw depth relation of CWP-11

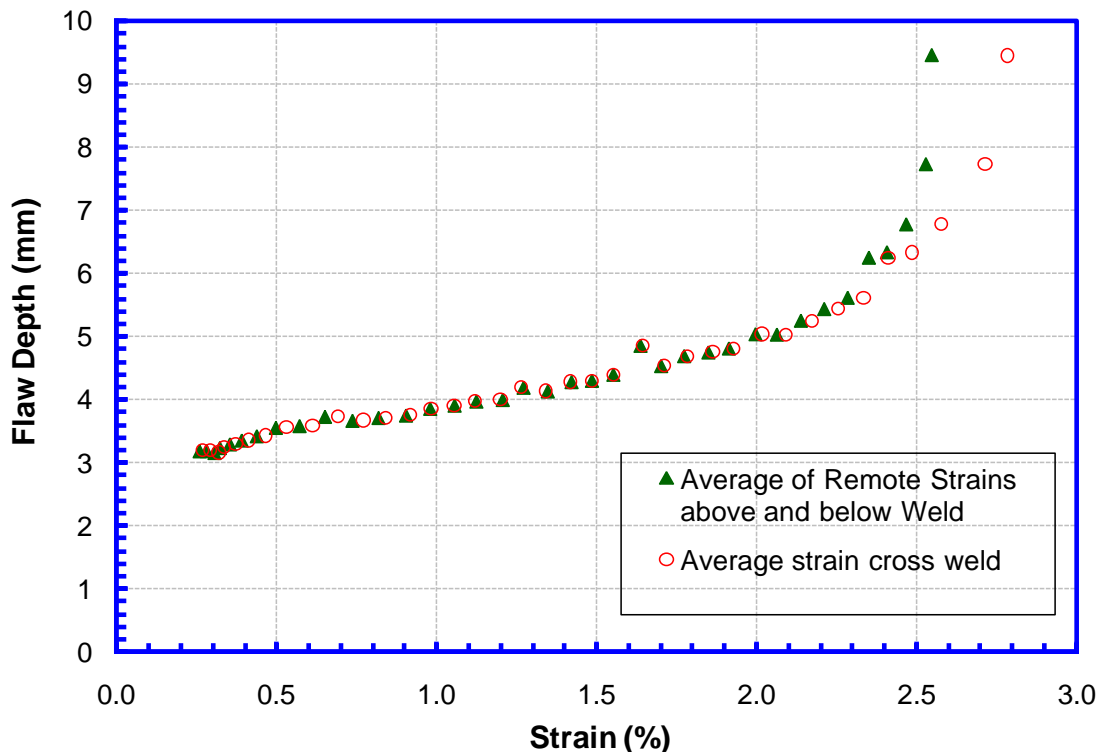


Figure 30: Flaw depth versus strains

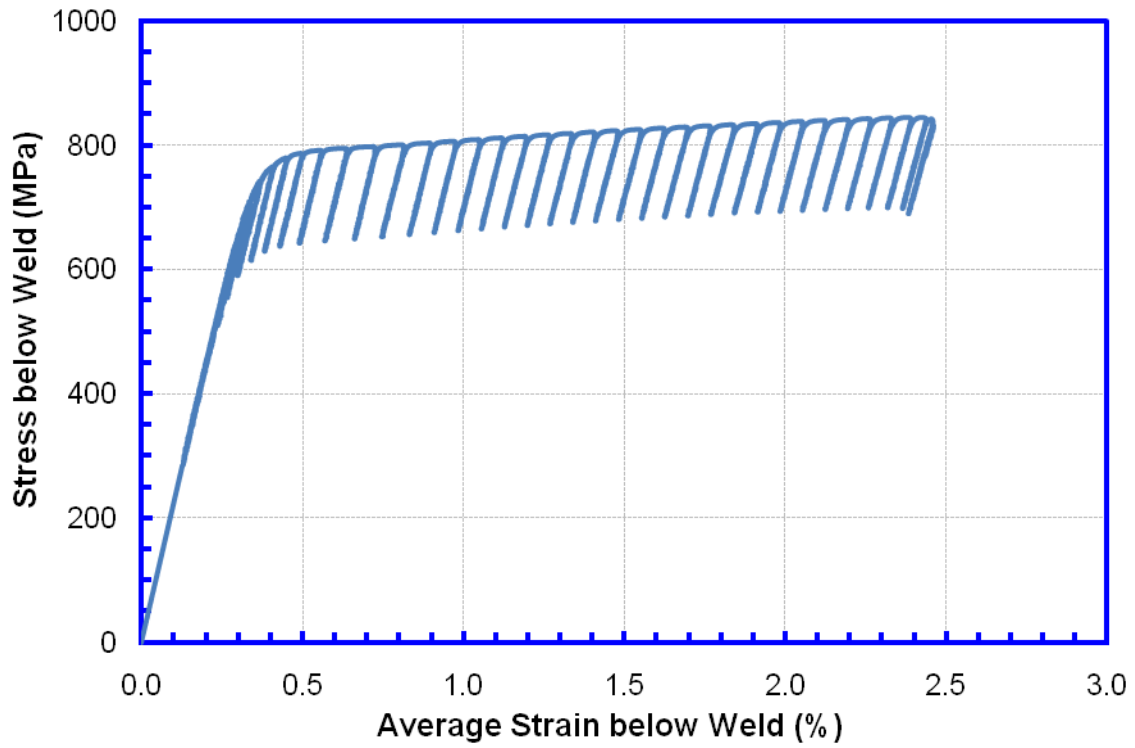


Figure 31: Stress versus average strain below the weld of CWP-11

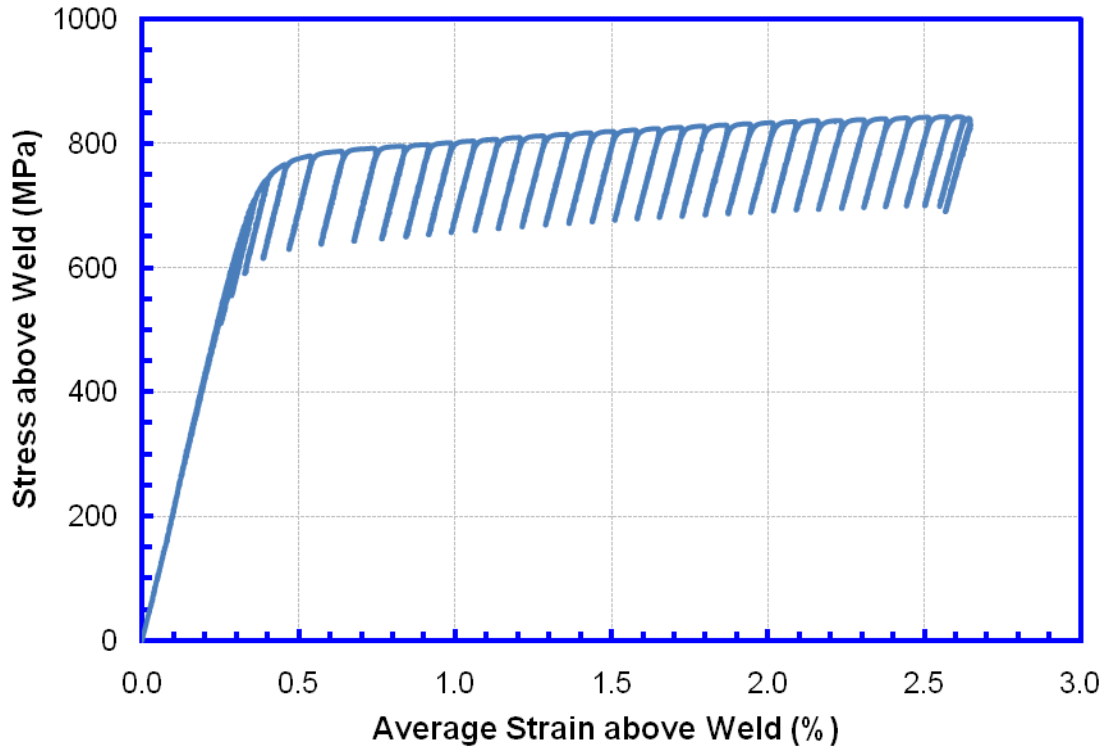


Figure 32: Stress versus average strain above the weld of CWP-11

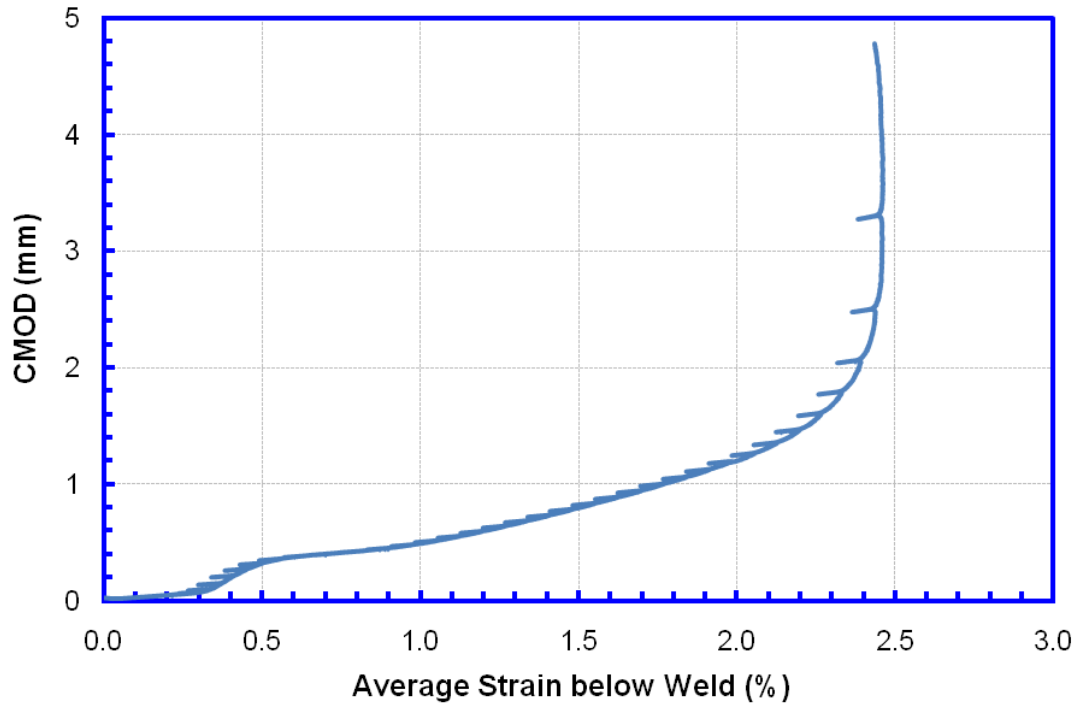


Figure 33: CMOD versus average strain below the weld of CWP-11

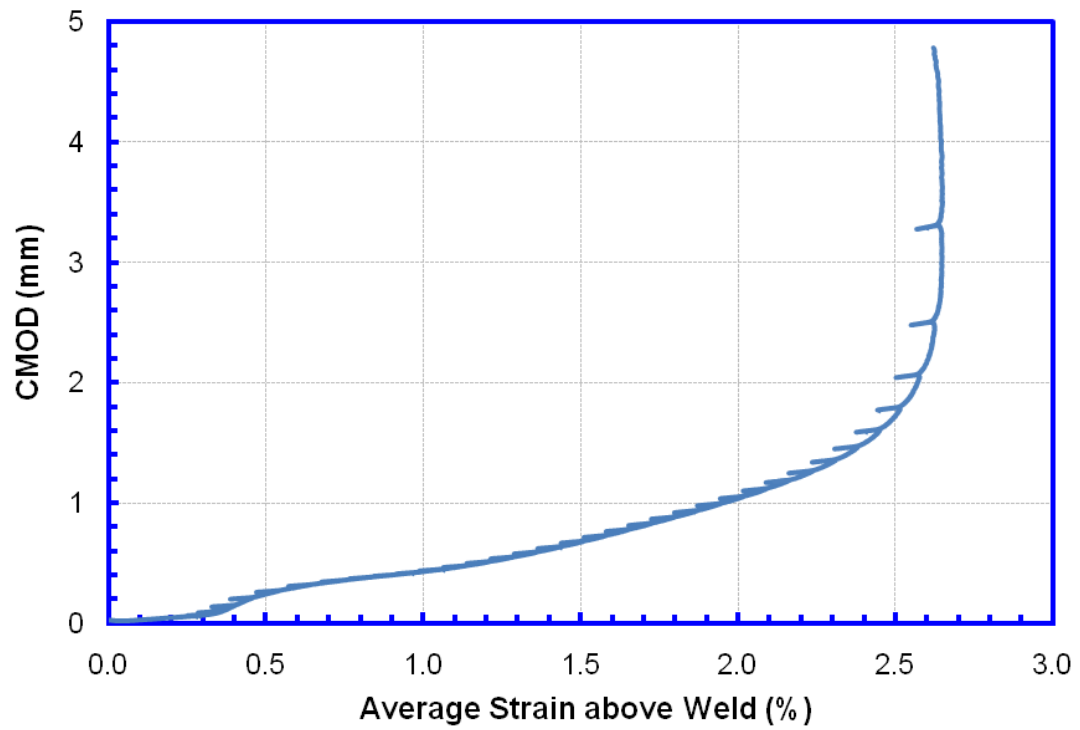


Figure 34: CMOD versus average strain above the weld of CWP-11

### 6.2.10 Average Stress vs. Average Strain

The stress-strain relations in the pipe sections remote from the weld may be derived from the LVDT measurements. Figure 31 shows stress versus average strain below the weld of CWP-11 and Figure 32 shows stress versus average strain above the weld.

### 6.2.11 CMOD versus Average strain

Figure 33 shows the CMOD versus average strain below the weld of CWP-11 and Figure 34 shows CMOD versus average strain above the weld.

### 6.2.12 Flaw Growth Resistance Curve

The  $J$  integral was calculated from flaw depth, load and CMOD data using  $J$ -correlation equations. The elastic component of the  $J$  integral was calculated from Equations (7) and (10)-(12). For each adjacent two pairs of load and CMOD data  $i-1$  and  $i$ , the increment of the plastic area under the load-CMOD curve  $A_{pi}^{i-1,i}$  was calculated using Equation (15). With Equation (13) for  $\eta$  factor at step  $i$ , the plastic component of the  $J$ -integral at step  $i$  was calculated from Equation (16). The  $J$  integral, from Equation (6), is the summation of the elastic component and the plastic component. The flaw growth was then obtained as  $\Delta a = a - a_0$ , where  $a_0$  is the calculated initial flaw depth. From Table 6,  $a_0 = 3.19$  mm for CWP-11 specimen. The relation between extent of flaw and  $J$ -integral, i.e., the fracture resistance curve of CWP-11, is developed and shown in Figure 35.

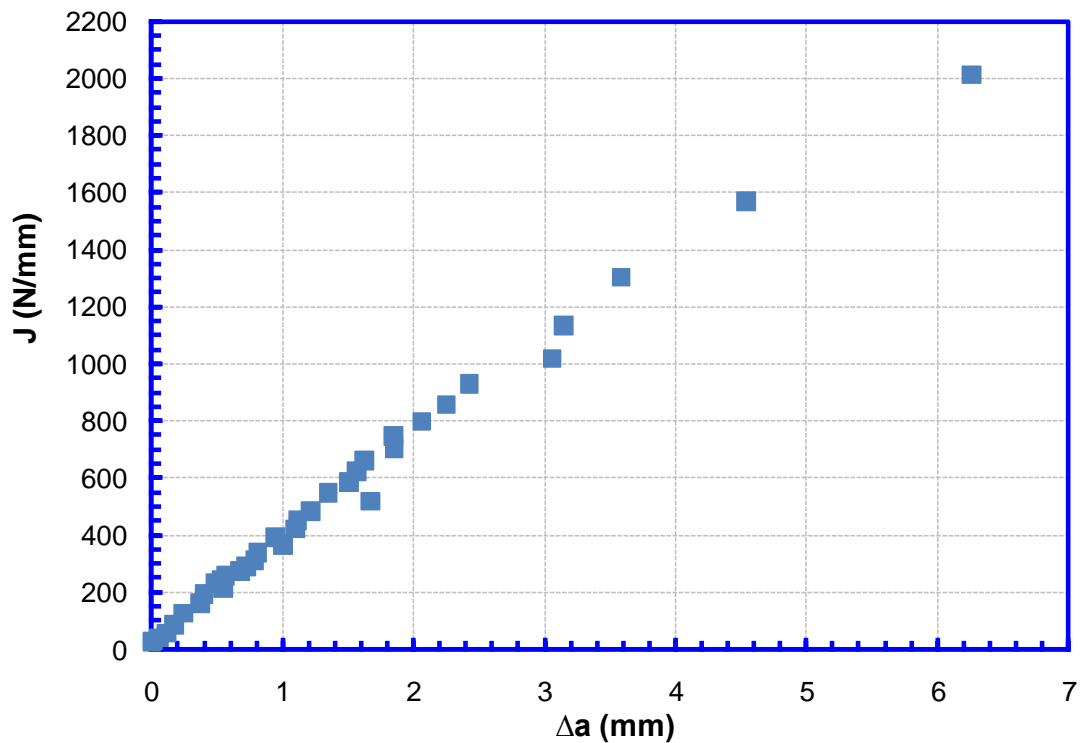


Figure 35: Fracture resistance curve of CWP-11

### 6.2.13 CMOD versus Applied Stress

The applied stress was calculated by dividing the load by the CWP cross-section area. Figure 36 shows the relation between the CMOD and the applied stress.

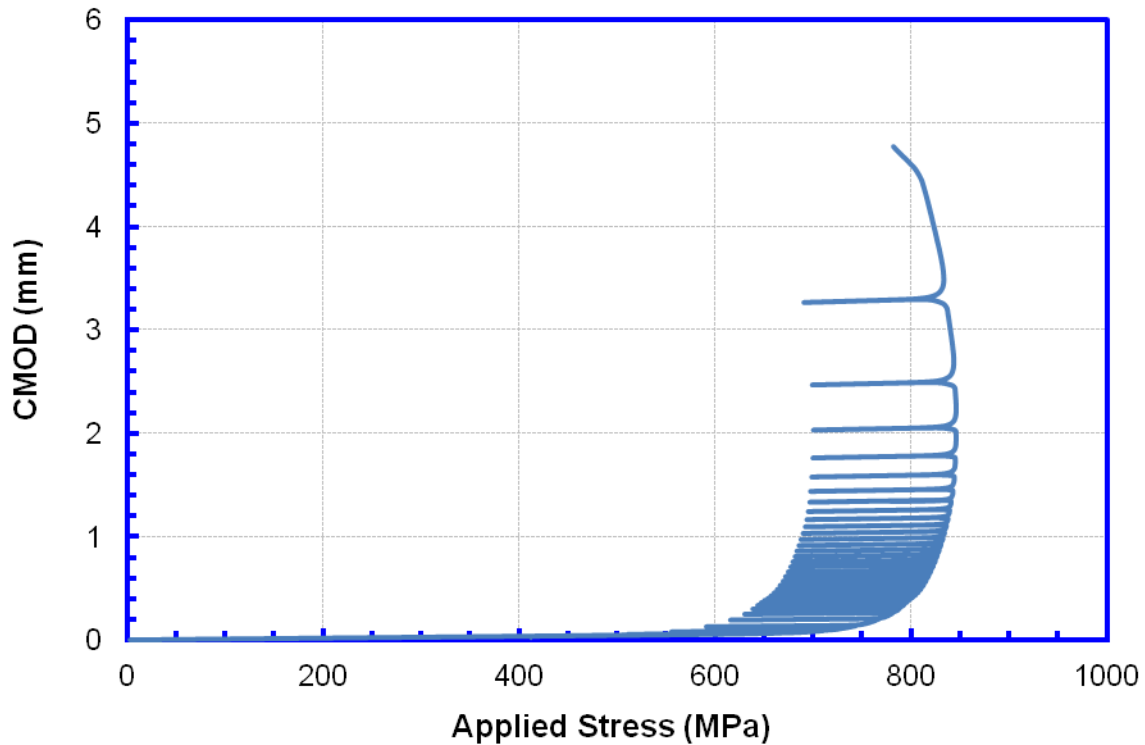


Figure 36: CMOD versus applied nominal stress of CWP-11

## 6.3 SUMMARY OF TEST DATA

The test data of a total of 34 CWP specimens were processed. Among those tests, 6 tests were performed at  $-40^{\circ}\text{C}$ , 17 tests were performed at  $-20^{\circ}\text{C}$  and 11 tests were performed at room temperature. Surface breaking flaws were created in weld centerline (16 tests), HAZ (16 tests) or base metal (2 tests) of the specimens. Four different dimension combinations of the flaws were adopted ( $a \times 2c$ : 2.0 mm  $\times$  75.0 mm in 4 tests, 2.5 mm  $\times$  50.0 mm in 4 tests, 3.0 mm  $\times$  50.0 mm in 18 tests and 6.0 mm  $\times$  30.0 mm in 8 tests).

The raw data collected from experiments were converted to a variety of measures of material behavior. The compliance function and  $J$  correlation equations were used to process the data into fracture resistance curves.

The analysis of the data has led to the following conclusions:

- 1) The CMOD vs. remote strain relation provides a useful indication of the start of accelerated flaw growth approaching the maximum achievable strains.
- 2) It is possible to generate resistance curves from the CWP tests with the developed compliance function and  $J$  correlation equations. However there can be considerable scatter in compliance measurements, leading to scatter in predicted flaw growth.

## 7 COMPARISON OF RESISTANCE CURVES

### 7.1 OVERALL ORGANIZATION OF THE DATA

The CWP resistance curves are compared with those from the SENT tests by CANMET. The summary of the comparison is organized in an electronic format. The experimental data are divided into 24 groups by the following parameters:

- 1) Round of weld,
- 2) Notch location, either in weld or in HAZ,
- 3) Notch depth, and
- 4) Test temperature.

The grouping of the data is listed in Table 8. In each comparison figure, the resistance curves of SENT specimens and CWP specimens with same geometric and test parameters are plotted.

### 7.2 SAMPLE RESISTANCE CURVE COMPARISON

Figure 37 shows three resistance curves from SENT tests with  $a=6$  mm weld flaw and test temperature  $T=-20^{\circ}\text{C}$ . The consistency of the three resistance curves is very good. Figure 38 shows one resistance curves from CWP test under the same test conditions. The comparison of the resistance curves from both sets of specimens is given in Figure 39. In all of these figures the filled symbols represent the data from SENT tests and the unfilled symbols represent the data from the CWP tests. The overall data trends show that the resistance curves of the CWP specimens are somewhat higher than those of SENT specimens after approximately 1.0 mm of flaw growth.

Similar comparison has also been done on HAZ flaws. Figure 40 shows two resistance curves from SENT tests with  $a=3$  mm at room temperature (RT). Figure 41 shows one resistance curve from a CWP test under the same test conditions. The flaw growth deduced from the unloading compliance shows a significant amount of scatter in the initial stage of flaw growth. Comparison of these resistance curves in Figure 42 demonstrates that the resistance curve of the CWP specimen agrees well with those of SENT specimens at small flaw growth (less than 0.5 mm). The CWP resistance becomes lower than that of SENT at greater flaw growth.

Examination of the weld cross section (Figure 43) indicates that the HAZ flaw was within the targeted HAZ region at the early stage of growth. The flaw then turned to the weld-HAZ fusion boundary and eventually propagated along the fusion boundary. The lower resistance beyond 0.5 mm flaw growth could be a reflection of the low fracture resistance along the fusion boundary or the change of growth direction which is not captured in the compliance function developed from finite element analysis. Figure 44 shows the weld cross section of CWP-27 specimen which has an HAZ flaw that did not reach the fusion boundary during its propagation. Figure 45 shows the comparison of the resistance curve of CWP-27 and those from SENT tests under the same test conditions. The overall data trends show that the resistance curve of the CWP specimen is higher than that of the SENT specimens after approximately 1.5 mm flaw growth. The initial part of the CWP resistance curve is very noisy so establishing a general trend is difficult.

**Table 8: Summary of SENT resistance curve versus CWP resistance curve**

Round of Welding	Flaw Location	Target Final Flaw Depth (mm)	Test Temperature (°C)	SENT Specimen ID	CWP Specimen ID
1	HAZ	3.0	-40	HZLT4K26, HZLT4K27	CWP-17, CWP-18
			-20	HZLTK08, HZLTK09, HZLTK16	CWP-02, CWP-05
			RT	HZRTK07	CWP-03
		6.0	-40	N/A	N/A
			-20	HZLTK05, HZLTK06, HZLTK17	CWP-12
			RT	HZRTK18, HZRTK20	CWP-15
	Weld	3.0	-40	WMLT4K24, WMLT4K25	CWP-13, CWP-14
			-20	WMLTK02, WMLTK15, WMLTK23	CWP-11, CWP-19
			RT	WMRTK01	CWP-16
		6.0	-40	N/A	N/A
			-20	WMLTK12, WMLTK13, WMLTK14	CWP-10
			RT	WMRTK11, WMRTK19	CWP-01
2	HAZ	3.0	-40	N/A	CWP-28
			-20	HZLTF06, HZLTF13	CWP-23
			RT	HZRTF05, HZRTF14	CWP-21
		6.0	-40	N/A	N/A
			-20	HZLTF08, HZLTF28	CWP-27
			RT	HZRTF07, HZRTF16	CWP-25
	Weld	3.0	-40	N/A	CWP-29
			-20	WMLTF10, WMLTF102	CWP-22
			RT	WMRTF02, WMRTF09	CWP-20
		6.0	-40	N/A	N/A
			-20	WMLTF03, WMLTF12	CWP-26
			RT	WMRTF04, WMRTF11	CWP-24

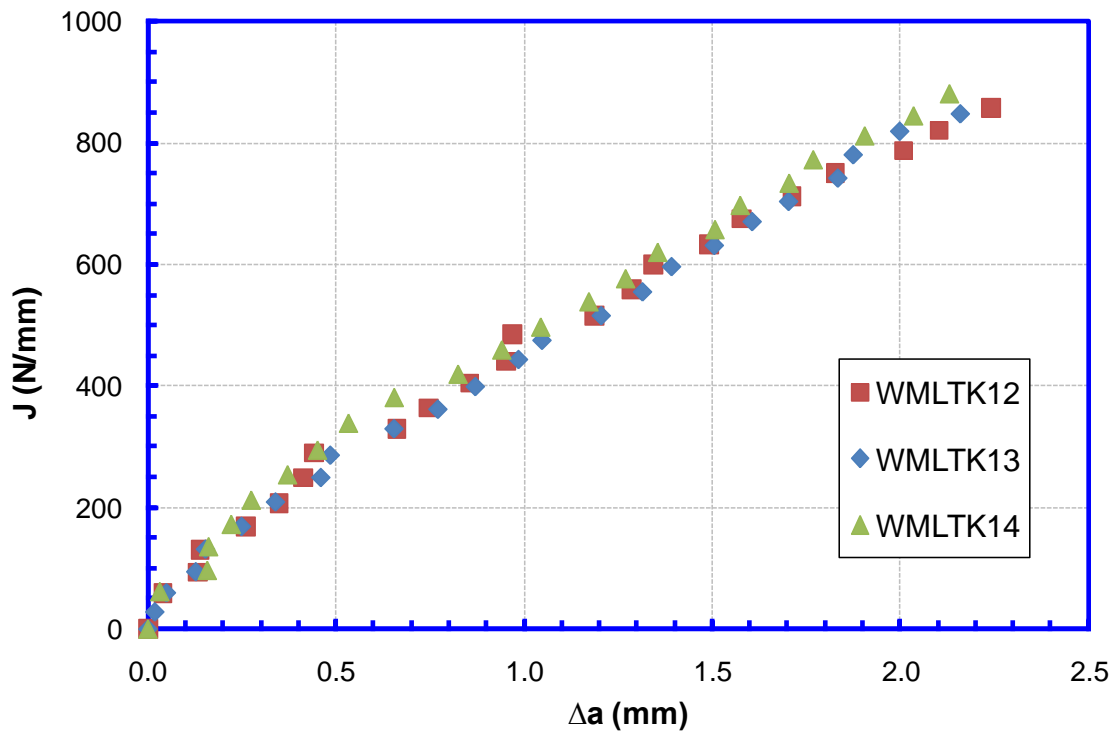


Figure 37: SENT resistance curves of the first round of welds, notch located in the weld metal,  $a=6$  mm and  $T=-20$  °C

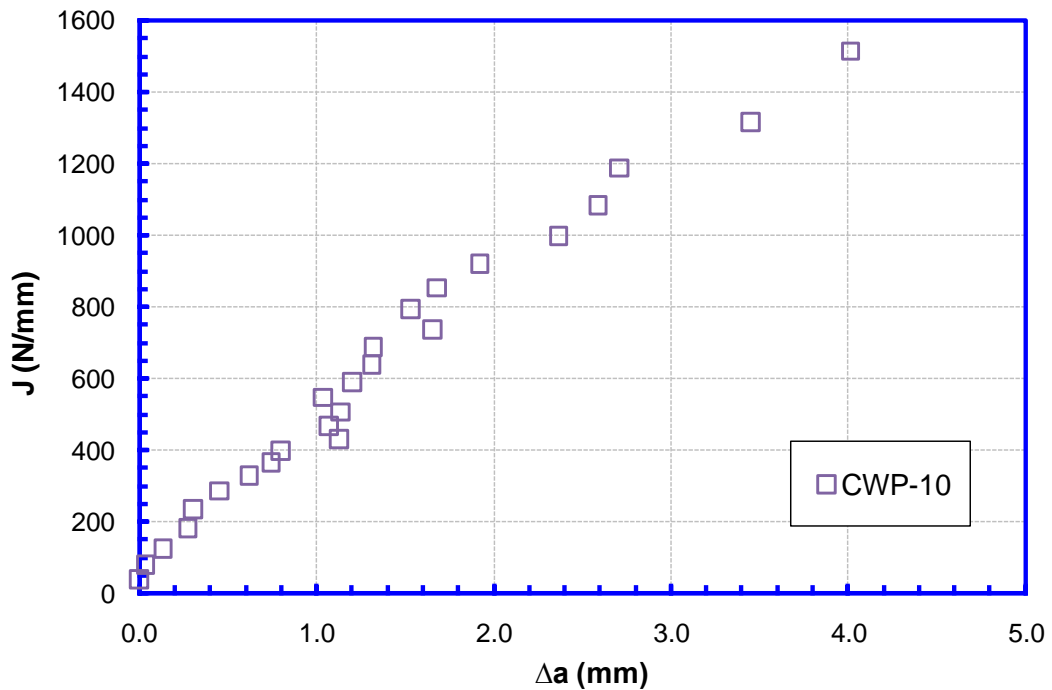


Figure 38: CWP resistance curves of the first round of weld, notch located in the weld metal,  $a=6$  mm and  $T=-20$  °C

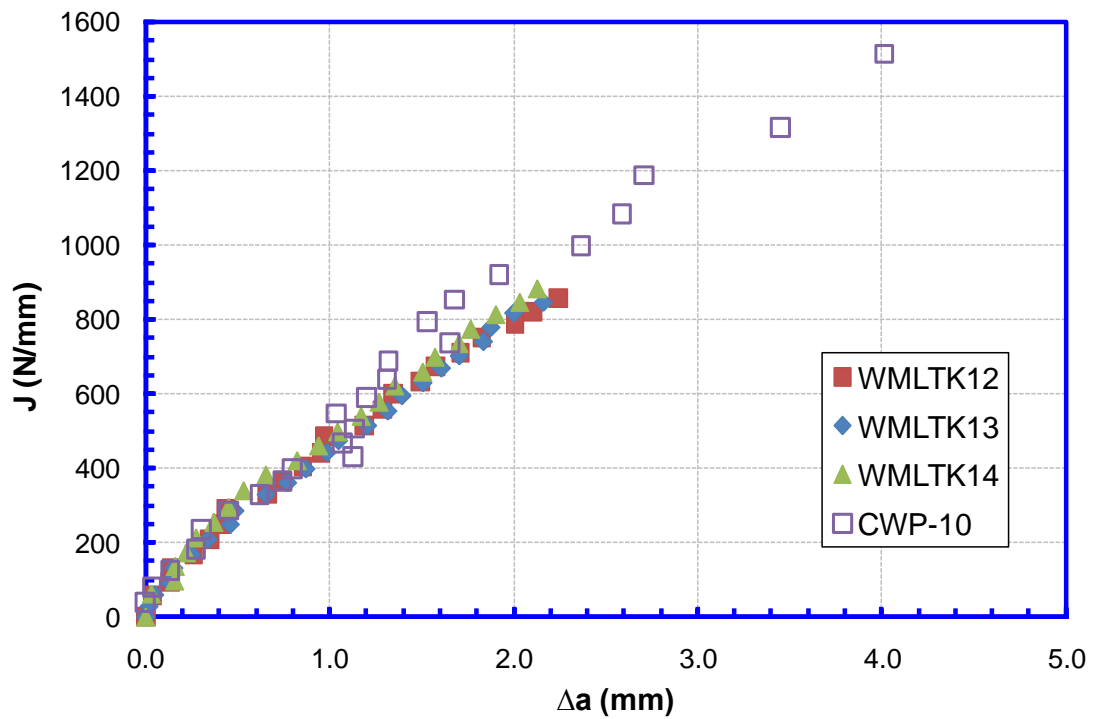


Figure 39: CWP resistance curves versus SENT resistance curves of the first round of weld, weld notch, a=6 mm and T=-20 °C

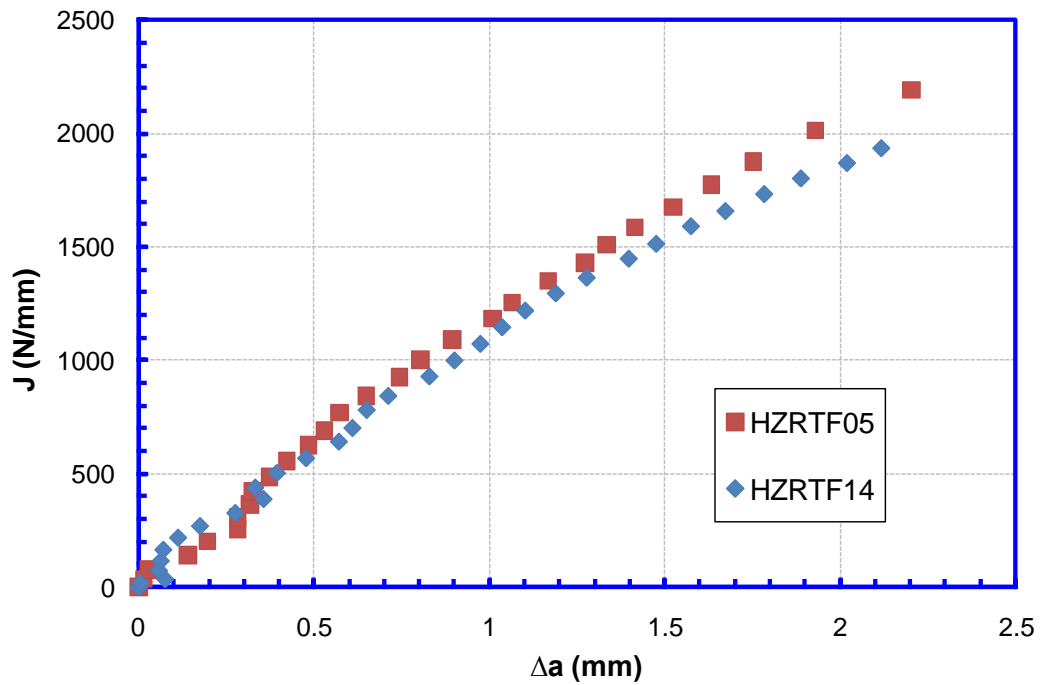


Figure 40: SENT resistance curves of the second round of weld, HAZ notch, a=3 mm and T=RT

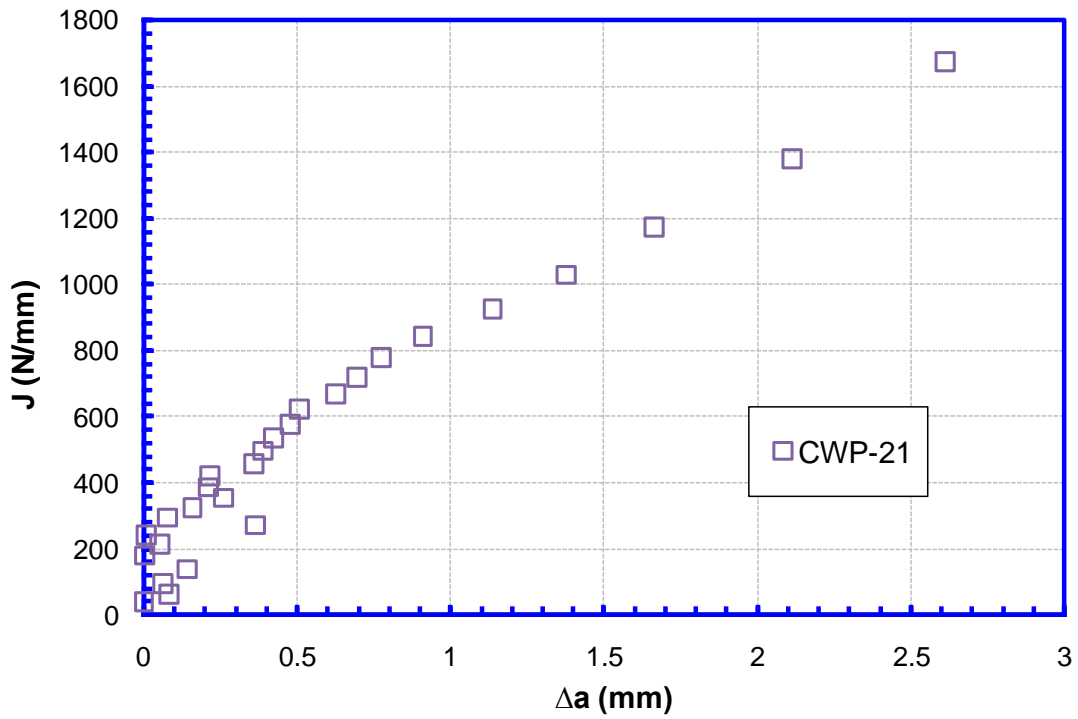


Figure 41: CWP resistance curves of the second round of weld, HAZ notch,  $a=3$  mm and  $T=RT$

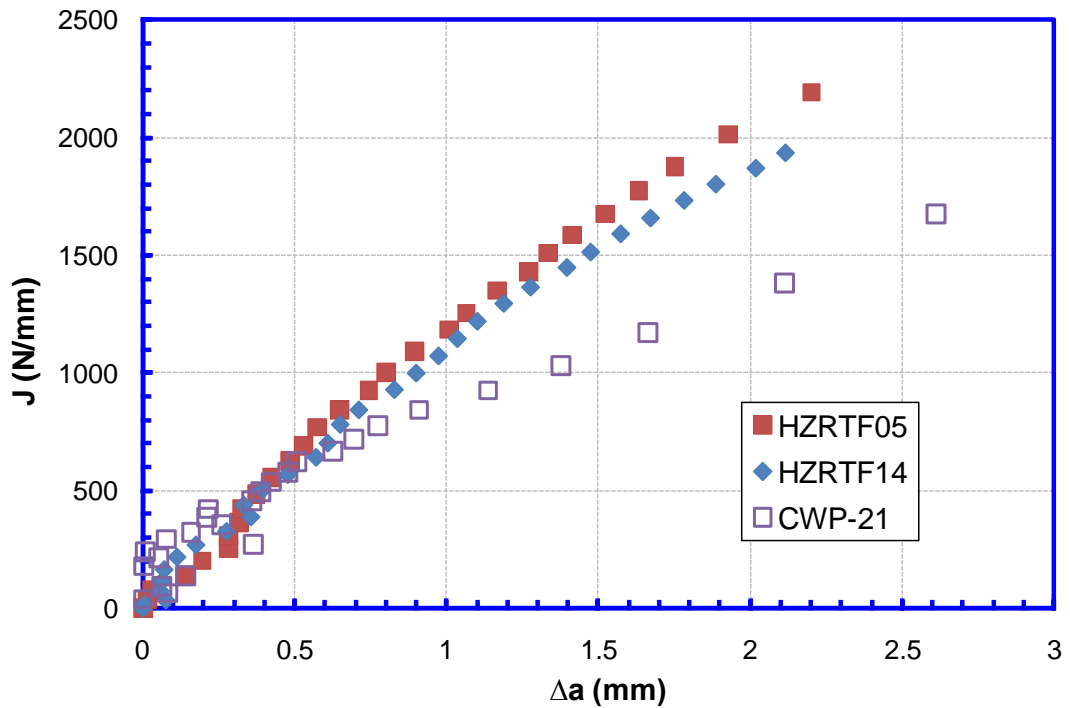
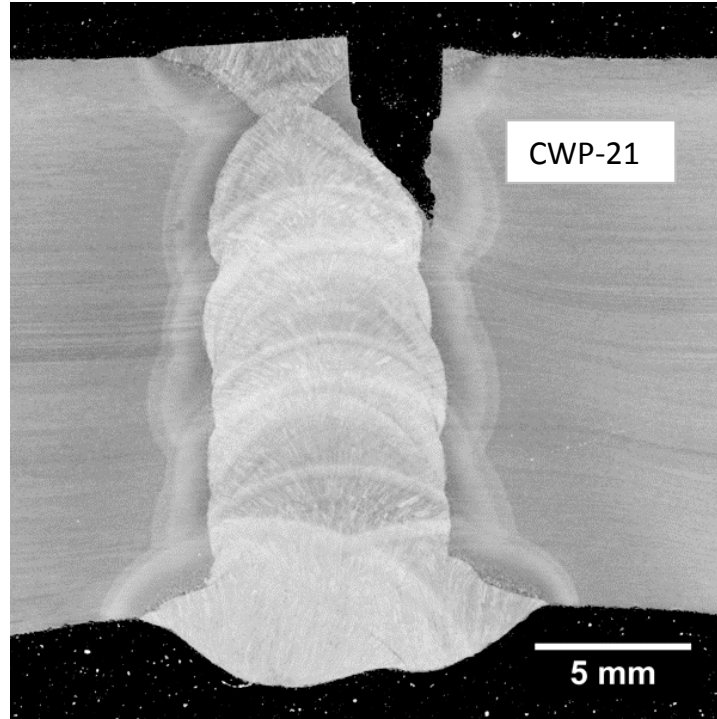
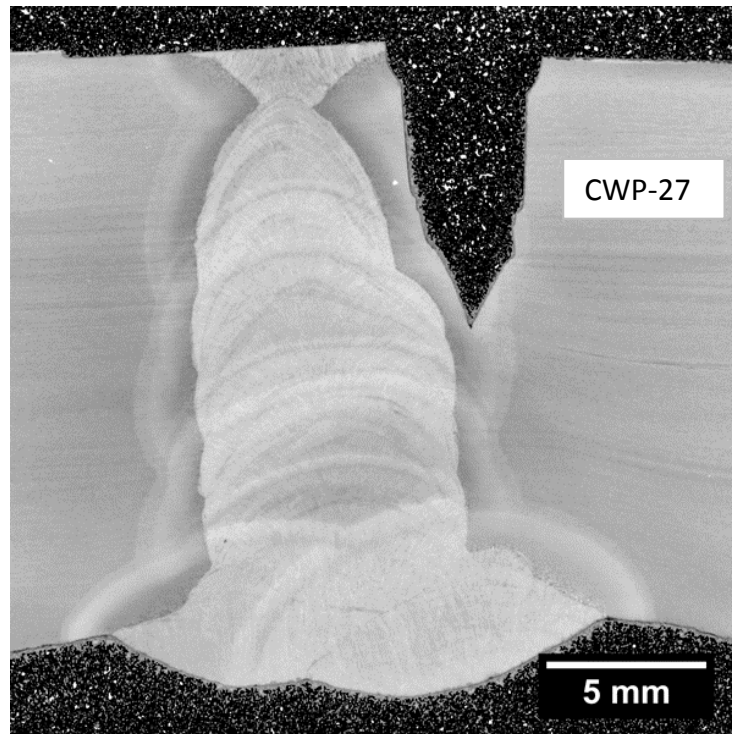


Figure 42: CWP resistance curves versus SENT resistance curves of the second round of weld, HAZ notch,  $a=3$  mm and  $T=RT$



**Figure 43:** After-test weld cross section macro of CWP-21 of the second round of weld, HAZ notch, a=3 mm and T=RT



**Figure 44:** After-test weld cross section macro of CWP-27 of the second round of weld, HAZ notch, a=6 mm and T=-20 °C

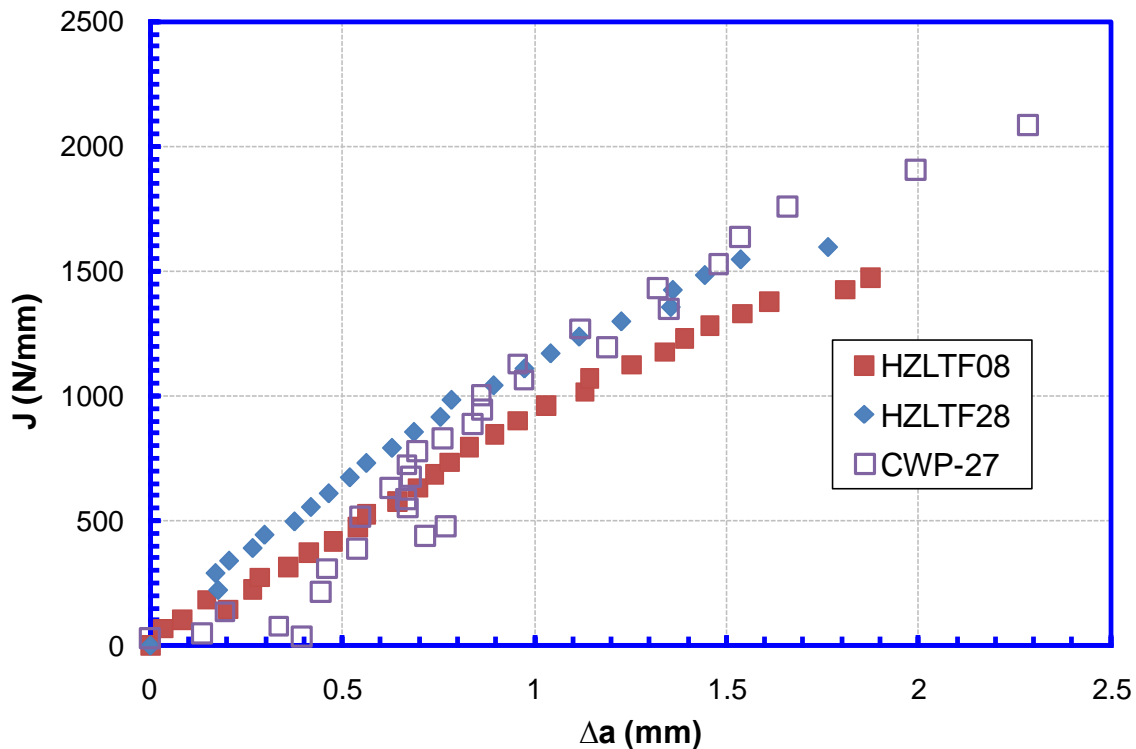


Figure 45: CWP resistance curves versus SENT resistance curves of the second round of weld, HAZ notch,  $a=6$  mm and  $T=-20$  °C

## 8 CONCLUDING REMARKS

Mechanical tests of different scale are often conducted to characterize and/or validate girth weld performance. Most of the tests are done in small-scale, i.e., with specimen size in the range of a few to tens of inches. Selected full-scale tests are sometimes done, often under special circumstances to understand the impact of certain parameters that cannot be incorporated into the small-scale tests. The medium-scale tests, represented by curved-wide-plate (CWP) tests, offer certain advantages associated with full-scale tests at a fraction of the cost of full-scale tests.

A large number of CWP tests were conducted within this project. The experimental procedures followed well-thought-out procedures only recently put into practice [18,19,20]. For post-test data analysis, there are no established procedures to generate resistance curves from CWP specimens. The two critical missing elements are (1) compliance function for estimating flaw growth from unloading compliance and (2) correlation equations to convert load vs. CMOD records to fracture mechanics parameters, such  $J$ -integral. These two elements are developed and presented in this report. With those two elements in place, resistance curves from CWP can be constructed. Another major outcome of this work is the implementation of a uniform data presentation format for all CWP test data.

The observation of the test data has shown the following.

- 1) It is possible to obtain highly consistent data representing the deformation of CWP specimens.
- 2) The remote strains obtained from the regions above and below the girth weld can be different, sometimes by a large amount. The difference in applied stress in those regions is minimal. The difference in strains is attributable to slight variations in material properties [21].
- 3) Based on the compliance and flaw growth history data, most of the flaw growth observed after the termination of a test occurs near the final failure strain. The amount of flaw growth at a strain level up to 90% of the final failure strain is a small fraction of the flaw growth at failure.
- 4) Once the flaw growth starts to accelerate, the remaining additional strain capacity is limited.
- 5) From a practical viewpoint of tensile strain design, it is advisable to use flaw growth initiation as a failure criterion. The benefits of a small increase in strain capacity do not justify the risk associated with allowing a large amount of flaw growth.
- 6) Despite a highly diligent and meticulous effort of post-test data processing, the scatter in the experimentally measured compliance of CWP specimens makes it difficult to construct “clean” resistance curves in some cases. This difficulty is particularly pronounced in the initial part of the resistance curves. Moreover, the initial flaw size predicted by the compliance function is in most cases different from the actual physical size. Some adjustments of the initial flaw size have to be made. These adjustments, along with the scatter in compliance, make the final determination of resistance curves somewhat subjective.
- 7) With the above stated difficulties in mind, comparison of the resistance curves between CWP and SENT tests were made. For cases when “clean” resistance curves can be established, the resistance curves from CWP tests are higher than those from SENT tests. The difference is more pronounced after a flaw growth of approximately 1.0 mm. Due to the noise associated with the initial flaw growth, comparison of resistance curves at smaller amount of flaw growth is difficult.
- 8) Post-test data processing for the generation of resistance curves can be a difficult task. The process can be subjected to the judgment calls of the individuals who process the data. The use of resistance curve data should be preceded with clearly defined procedures for data processing. The robustness of the raw data prior to the data processing should be examined and verified.
- 9) In light of comments nos. 6 and 8, considerable skill and care is needed in the instrumentation of the specimens and data interpretation to generate reliable resistance curves from CWP specimens.
- 10) More work is needed to fully understand the CWP test results and their correlation with the test data of smaller scale specimens, such as SENT. Such work is being planned by this project group.

## 9 REFERENCES

---

- 1 Denys, R., “Weld Plate Testing of Weldments, Part I, II, and III, Fatigue and Fracture Testing of Weldments,” ASTM STP 1058, pp. 157-228. ASTM, Philadelphia, 1990.
- 2 Denys, R., Lefevre, A. A., Glover, A., G., “Weld Metal Yield Strength Variability in Pipeline Girth Welds,” Second Pipeline Technology Conference, Ostend, Belgium, 1995, Vol. II, pp.591-598.
- 3 Wang, Y.-Y., Liu, M., Stephens, M., Petersen, R., and Horsley, D., “Recent Development in Strain-Based Design in North America,” Proceedings of the 19<sup>th</sup> International Offshore and Polar Engineering Conference (ISOPE 2009), Osaka, Japan, July 21-26, 2009.
- 4 Denys, R., Lefevre, A., and Baets, P. D., “A Rational Approach to Weld and Pipe Material Requirements for a Strain Based Pipeline Design,” Proceedings of Applications & Evaluation of High-Grade Linepipes in Hostile Environments, Pacifico Yokohama, Japan, pp. 121-157, November 7-8, 2002.
- 5 Wang, Y.-Y., Liu, M., Chen, Y., and Horsley, D., “Effects of Geometry, Temperature, and Test Procedure on Reported Failure Strains from Simulated Wide Plate Tests,” 6<sup>th</sup> International Pipeline Conference, Paper No. IPC2006-10497, September 25-29, 2006, Calgary, Alberta, Canada.
- 6 Østby, E., “Fracture Control-Offshore Pipelines - New Strain-Based Fracture Mechanics Equations Including the Effect of Biaxial Loading, Mismatch, and Misalignment,” Proceedings of 24<sup>th</sup> International Conference on Offshore Mechanics and Arctic Engineering, Kalkidiki, Greece June 12-17, 2005.
- 7 Cheng, W., Tang, H., Gioielli, P., Minnaar, K., Macia, M., “Test Methods for Characterization of Strain Capacity: Comparison of R-Curves from SENT/CWP/FS Tests,” Pipeline Technology Conference, 12-14 October 2009, Ostend, Belgium.
- 8 DNV/SINTEF/TWI, “Fracture Control for Installation Methods Introducing Cyclic Plastic Strains, Development of Guidelines for Reeling of Pipelines,” a JIP performed jointly by DNV, SINTEF, and TWI.
- 9 Shen, G., Gianetto, J. A., Tyson, W. R., “Measurement of J-R Curves Using Single-Specimen Technique on Clamped SE(T) Specimens,” Proc. 19th Intl. Offshore and Polar Eng. Conf., ISOPE, 2009, pp. 92–99.
- 10 Wang, Y.-Y., Liu, M., and Song, Y., “Second generation models for strain-based design,” final report to US DOT and PRCI, US DOT contract No. DTPH56-06-T000014, August 30, 2011.
- 11 Hukle, M. W., Horn, A. M., Hoyt, D. S., and LeBleu, Jr., J. B., “Girth Weld Qualification for High Strain Pipeline Applications,” *Proceeding of the 24<sup>th</sup> International Conference on Offshore Mechanics and Arctic Engineering*, June 13-17, Kalkidiki, Greece.
- 12 Denys, R., Lefevre, A., and Baets, P. D., “A Rational Approach to Weld and Pipe Material Requirements for a Strain Based Pipeline Design,” *Proceedings of Applications & Evaluation of High-Grade Linepipes in Hostile Environments*, Pacifico Yokohama, Japan, November 7-8, 2002, pp. 121-157.
- 13 Denys, R.M. and Lefevre A.A., “UGent guidelines for curved wide plate testing”, *Pipeline Technology Conference*, Paper number Ostend2009-110, Ostend, Belgium, October 12-14, 2009.

- 
- 14 Weeks, T. and Richards, M., "Curved Wide Plate Tests," PHMSA Agreement No. DTPH56-07-0001, Topical Report 277-T-09, December 2011.
  - 15 Kirk, M. T. and Wang, Y.-Y., "Wide Range CTOD Estimation Formulae for SE(B) Specimens," in *Fracture Mechanics, 26th Volume*, ASTM STP 1256, W. G. Reuter, J. J. Underwood, and J. C. Newman, Jr., Eds., ASTM, 1995.
  - 16 Pisarski, H. G., Wang, Y.-Y., Kirk, M. T., and Gordon, J. R., "The Effect of Yield Strength Mismatch on CTOD and  $J$  Estimation Procedure for Weld Metal Fracture Toughness Determination," Proceedings of the 14th International Conference on Offshore Mechanics and Arctic Engineering, Copenhagen, Denmark, Volume III, 1995, pp. 427-434.
  - 17 ASTM Standard E 740, "Standard Practice for Fracture Testing with Surface-Crack Tension Specimens," ASTM *International*, Philadelphia, 2003.
  - 18 Wang, Y.-Y., Liu, M., Rudland, D., and Horsley, D., "Strain Based Design of High Strength Pipelines," Proceedings of the 17<sup>th</sup> International Offshore and Polar Engineering Conference (ISOPE 2007), Lisbon, Portugal, July 1-6, 2007.
  - 19 Wang, Y.-Y., Stephens, M., Horsley, D., "Preliminary Analysis of Tensile Strain Capacity of Full-Scale Pipe Tests with Internal Pressure," Proceedings of the 18<sup>th</sup> International Offshore and Polar Engineering Conference (ISOPE 2008), Vancouver, Canada, July 6-11, 2008.
  - 20 Stephens, M., Petersen, R., Wang, Y.-Y., and Horsley, D., "An Experimental Basis for Improved Strain-Based Design Models," Proceedings of the 19<sup>th</sup> International Offshore and Polar Engineering Conference (ISOPE 2009), Osaka, Japan, July 21-26, 2009.
  - 21 Wang, Y.-Y., Liu, M., Gianetto, J., and Tyson, B., "Considerations of Linepipe and Girth Weld Tensile Properties for Strain-Based Design of Pipelines," *Proceedings of the 8<sup>th</sup> International Pipeline Conference*, Paper No. IPC2010-31376, September 27 – October 1, 2010, Calgary, Alberta, Canada.